Bachelor thesis

Setup of a laser system for the excitation of nitric oxide from the $\mathsf{H}\,^2\Sigma^+, \mathsf{H}'\,^2\Pi$ state to Rydberg states

Michael Ilewicz

07 March 2020

A thesis submitted in fulfillment of the requirements
for the degree of a bachelor of physics at the

University of Stuttgart
Faculty 08
5th Institute of Physics
to Prof. Dr. Tilman Pfau

Eidesstattliche Erklärung

Hiermit versichere ich gemäß §24 Absatz 7 der Prüfungsordnung der Universität Stuttgart für den Bachelorstudiengang Physik vom 31. Juli 2015, dass ich diese Arbeit selbständig verfasst habe, dass ich keine anderen als die angegebenen Quellen benutzt und alle wörtlich oder sinngemäß aus anderen Werken übernommenen Aussagen als solche gekennzeichnet habe. Ich versichere, dass die eingereichte Arbeit weder vollständig noch in wesentlichen Teilen Gegenstand eines anderen Prüfungsverfahrens gewesen ist. Weiterhin versichere ich, dass das elektronische Exemplar mit dem Inhalt der Druckexemplare übereinstimmt.

Michael Ilewicz

Stuttgart, den 7. März 2020

Deutsche Zusammenfassung

Im Rahmen dieser Arbeit wurde ein Lasersystem bei einer Wellenlänge von 835 nm geplant und teilweise aufgebaut. Ein optischer Verstärker wurde aus Einzelteilen zusammengebaut und seine Steuereinheit kalibriert und aufgestellt. Eine Platine, die den Verstärker vor Überspannung, Verpolung und Versorgungsspitzen schützen soll, wurde gebaut und auf Funktionalität getestet. Anschließend wurden die optischen Elemente bis zum Verstärker aufgebaut und der zu verstärkende Laserstrahl in seiner Form angepasst.

Ein Fabry-Pérot Interferometer, welches als relative Wellenlängenreferenz genutzt wird, wurde nach dem Design von Christian Tomschitz [1] gebaut und nach seiner freien spektralen Bandbreite (free spectral range FSR) charakterisiert. Hierfür wurde die Durchlässigkeit des Interferometers zur gleichen Zeit gemessen wie das Absorptionsspektrum von ^{87}Rb. Mithilfe der Übergangsfrequenzen verschiedener elektronischer Zustände wurde die Bandbreite zu FSR = 935(43) MHz bestimmt. Da die Messung nichtlinear verläuft, kommt es zu einer großen Unsicherheit. Ein weiterer Ansatz war der Vergleich mit einem ultrastabilen (ultra low expansion ULE) Interferometer, dessen Bandbreite grob bekannt war. Dies ergab eine Bandbreite von 958(1) MHz, was implizieren würde, dass das Interferometer 3,5 mm kürzer als geplant wäre. Ein weiterer Ansatz wurde selbstständig entwickelt der die Messung des Absorptionsspektrums linearisierte und für die Bandbreite FSR = 940(2) MHz ergab. Ein Vergleich mit dem vorigen Ansatz zeigt, dass die Bandbreite des ULE Interferometers FSR = 1.471(6) GHz ist.

Ein Teil des zu verstärkenden Strahls wurde dann zu dem Fabry-Pérot Interferometer abgelenkt, ein weiterer Teil wurde zu einer Glasfaser geleitet, welche zu einem Wellenlängenmessgerät führt. Anschließend wurde versucht in den Verstärker einzukoppeln, jedoch ohne Erfolg. Nach einer langen Fehlersuche wurde schließlich festgestellt, dass die Verstärkerdiode beschädigt war und ersetzt werden musste. Mikroskopbilder vermitteln den Anschein, dass der Schaden thermischer Natur war, welcher bereits während dem Anlöten der Diode entstanden sein könnte. Unglücklicherweise konnte auch mit der neuen Diode der Verstärker nicht in Betrieb genommen werden. Es wurden mehrere Linsenkombinationen getestet, und alle uns bekannten möglichen Fehlerquellen untersucht. Während der Fehlersuche wurde ein Algorithmus zur schnellen und einfachen Kopplung des Lasers eingeführt, aber auch andere Ansätze führten zum gleichen Ergebnis: Nach einer ersten Strahlüberlappung wird ein Anstieg der emittierten Leistung beobachtet. Da dieses von der Polarität abhängt, konnten wir bestätigen, dass es sich hierbei nicht um reine Reflektion des

Strahls im Verstärker handelt. Nach vorsichtiger Optimierung konnten jedoch nie Laserleistungen größer als 80 % der Eingangsleistung erreicht werden. Eine mögliche Erklärung ist, dass die Linsenblockposition wichtiger ist als vermutet und noch nicht absolut perfekt eingestellt werden konnte. Ein möglicher Hinweis auf die korrekte Position könnte aus dem Verhalten des ASE unter einschrauben der Linsenröhre gegeben sein. Bei optimaler Position sollte sich das ASE dabei nicht bewegen. In der aktuellen Position wird hingegen eine Präzession des ASE beobachtet, was aber auch aus einer leichten Asymmetrie der Linse stammen könnte. Im Rahmen dieser Arbeit konnte dies jedoch nicht mehr weiter untersucht werden. Als Beispiel einer Charakterisierungsmessung wird stattdessen die Verstärkercharakterisierung eines funktionierenden Aufbaus vorgestellt.

In der nahen Zukunft werden andere Mitarbeiter weiter versuchen die Linsenblockposition richtig einzustellen und so, hoffentlich, eine Verstärkung erreichen. Sobald der Verstärker letztendlich aufgestellt werden konnte, sind alle drei Wellenlängen zur Detektion von Stickstoffmonoxid für den Spurengasnachweis vorhanden. Im nächsten Schritt muss ein Gasmischgerät realisiert werden, welches Stickstoff und Stickstoffmonoxid in bekannten Konzentrationen mischt. Dann muss ein Prototyp realisiert werden in welchem das Gasgemisch im Durchfluss durch die Laser angeregt wird und der durch den Zerfall von Rydbergzuständen entstehende Strom beobachtet werden kann.

Abstract

This thesis describes the setup of a laser system at 835 nm for the excitation of nitric oxide from excited states to Rydberg states. More specifically, the setup of the seed laser and the technical challenges of a tapered amplifier, such as protective measurements and controller calibration, are described. A strategic approach to coupling of this specific amplifier design as well as a little troubleshooting guide for tapered amplifiers is presented. Additionally, a reference cavity is characterized through comparison to the absorption spectrum of ^{87}Rb. Here, two numerical approaches that account for non-linearities in laser scanning during spectroscopy are presented.

Contents

1. Introduction

Nitric oxide (NO) plays an important role in the human immune system, as a neurotransmitter [2] and in many other biological processes [3]. NO can move between cell membranes where it regulates RNA and protein synthesis, promotes neurotransmission and controls gene expression [4]. However, due to its radical nature, excessive amounts of NO are neurotoxic and can facilitate early apoptosis [4]. Consequently, the detection of NO is of great interest in medicine, especially for the diagnosis of inflammatory diseases such as asthma [5] or as a signaling molecule for tumor growth [6]. Existing detection schemes such as the detection through chemiluminescence [7] suffer from cross sensitivities to other molecules and other technical difficulties.

A recent proof of concept study [8, 9] proposed a trace gas sensor based on Rydberg excitations which could overcome many problems of currently used methods. Ideally, the patient would only need to breath into a tube leading to a device and the current NO concentration within the human breath could be known almost immediately. In this approach, Rydberg states are optically excited in thermal NO. This means that the NO molecule is close to ionization and through collisions with other gas particles the Rydberg molecule decays into a pair of charges. Using two electrodes, these charges can then be measured and the amount of NO within the investigated gas can in theory be calculated.

This thesis is part of the attempt to realize such a Rydberg excitation at our institute based on a three-level excitation scheme. More specifically, the first two excitation levels have already been realized. The transitions from the ground state to A states $\mathrm{A}\,^2\Sigma^+ \leftarrow \mathrm{X}\,^2\Pi_{1/2}$ has been set up and first results are presented by Fabian Munkes in [10]. The second transition excites the NO from A states to H states $\mathrm{H}\,^2\Sigma^+ \leftarrow \mathrm{A}\,^2\Sigma^+$ and has been prepared by André Bisquerra [11]. The goal of this thesis is the setup of a laser system for the final excitation from the $\mathrm{H}\,^2\Sigma^+, \mathrm{H}'\,^2\Pi$ states to Rydberg states. This transition takes place at 835 nm. A diode laser at this wavelength is amplified using a tapered amplifier to achieve the optical power of up to 1 W necessary for the experiment.

2. Theoretical Background

In this section the theoretical background that is needed to understand why the laser system has been set up this way is presented. Additionally, we provide an overview of possible security precautions that can be met to protect the laser amplifier from damage and degradation and a small troubleshooting guide for this amplifier design. Finally, we present the necessary basics to understand the Fabry-Pérot interferometer which is used as a wavelength reference.

2.1. Tapered Amplifier

The excitation of nitric oxide into Rydberg states depends on sufficient excitation power. Commonly used, cost efficient diode lasers have the required precision, but often do not offer the required power in this price regime. A wide spread and relatively cheap device used to preserve the diode lasers spectral properties and increase the optical power sufficiently is the tapered amplifier (TA) [12]. It inherits its name from the tapered (widening) gain section which follows a short waveguide section (see figure 2.1). The waveguide section ensures that only the fundamental transverse mode is excited [12]. The dimensions of TA-chips typically don't differ much [12]. The waveguide has a width w_1 of around $1 - 3\,\mu$m ($3\,\mu$m in this case) in which the laser light that is to be amplified (seed laser) must be carefully introduced. The gain section then widens up to $w_2 \sim 200\,\mu$m ($200\,\mu$m in this case) with a taper angle θ of about 6° which allows for the beam to diffract and fill the entire gain section with the single mode light and therefore emit the desired photons in the entire gain region. To dissipate unwanted oscillating modes, two cavity-spoiling grooves are etched into the chip outside of the active region.

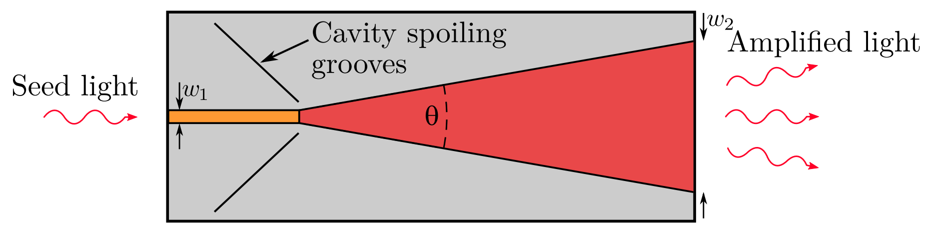

Figure 2.1.: Top view of a TA-chip showing the waveguide with width w_1 and the tapered gain region with tapering angle θ and an output aperture of w_2.

2.1.1. Physical process

In order to explain the process of amplification inside the TA-chip, we can describe the gain medium as a two-level system, considering a lower state $|L\rangle$ and an excited state $|E\rangle$ [13]. When applying an external voltage, electrons from the lower state $|L\rangle$ are lifted into the excited state $|E\rangle$. Electrons in this state can decay spontaneously, emitting a photon with a polarization and frequency solely related to the exact nature of the excitation state $|E\rangle$. This process is referred to as "amplified spontaneous emission" (ASE). Conversely, a photon from the seed laser can stimulate the decay from $|E\rangle$ to $|L\rangle$, again emitting a photon but now with a mode identical to that of the seed photon. A schematic of this process is shown in figure 2.2. Photons from both processes propagate through the medium, creating an avalanche effect which is emitting more and more photons, amplifying the initially stimulating light.

However, only the photons stimulated by the seed laser are of any use. To ensure the maximal output of such light, the gain section begins with the width of the waveguide, which leads to a very high power density in this area. This ensures, that almost all excited electrons are decaying in causality of the seed stimulation, so that few are left which can decay spontaneously [13]. The avalanche effect than causes the high initial density to travel across the whole length and width of the gain medium as depicted in figure 2.3. This minimizes the amount of spontaneous emissions, while maximizing stimulation from seed photons.

It is important to note, that the two-level system is sufficient to understand the basic concept but is a strong oversimplification. A better, more complex description would be a four-state system with an additional ground state and a reservoir state, which is described in more detail for example in [14].

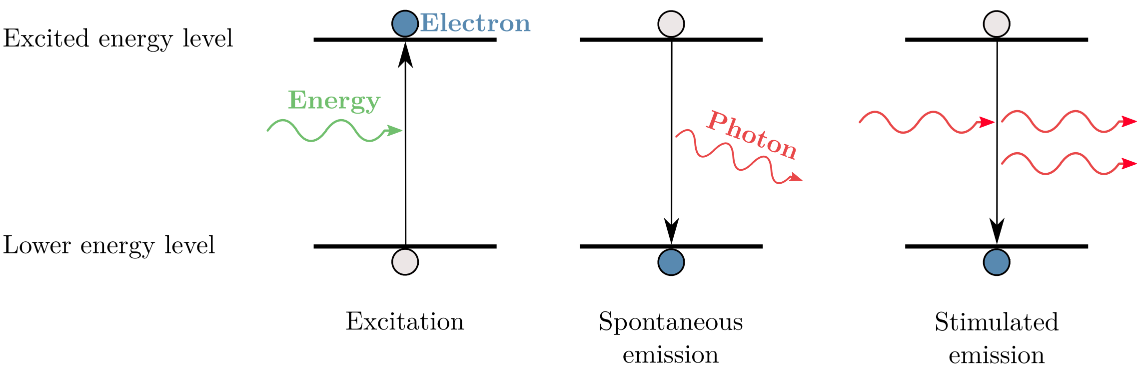

Figure 2.2.: Schematic energy diagram of the two-level emission process in the tapered amplifier.

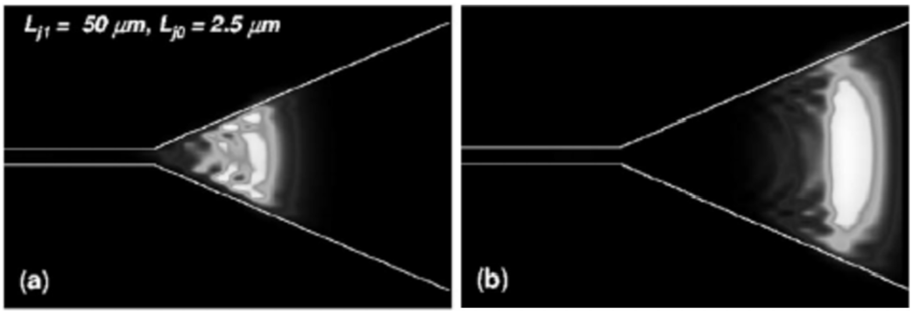

Figure 2.3.: Propagation of a picosecond pulse in a tapered amplifier [15].

2.1.2. TA handling and safety

As the TA-chip is highly sensitive, precautions must be met to protect the chip from destruction. Possible sources of permanent damage or degradation and the corresponding precautions have been described in [12] and are summarized in this chapter. An overview is presented in table 2.1. During the setup, contact of the facet or the pumping wires with any object will immediately leave the chip unusable. Furthermore, overheating during soldering is an important factor. Soldering should be done as **quick as possible** because heat leads to degradation of the chip and can cause complete destruction. The first TA-chip that was ordered for this thesis could not be coupled successfully. After examination of the chip facet under the microscope, damage has been found. The images shown in figure 2.4 suggest that the damage is of thermal nature, as it is located directly over the pumping wires. We suspect that this damage resulted from soldering too long and too often.

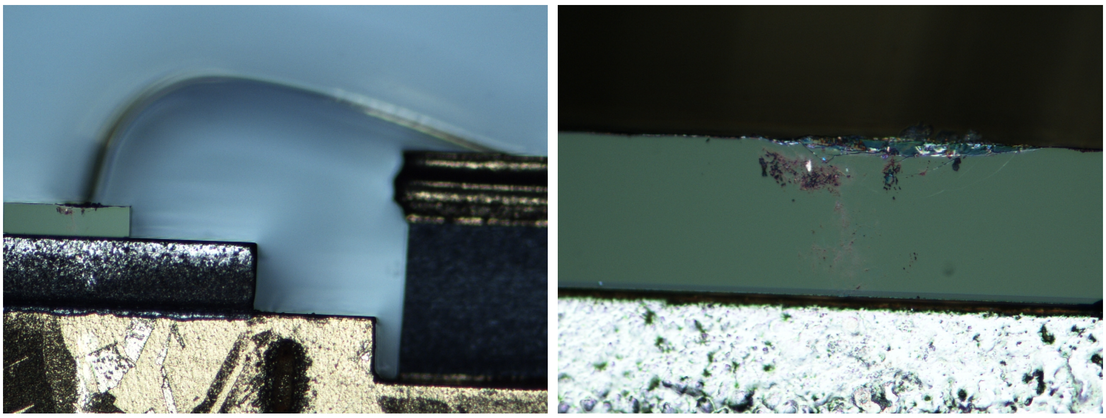

(a) 4x magnification **(b)** 20x magnification

Figure 2.4.: Microscope pictures of the defective TA-chip.

Another source of permanent damage can be a light beam hitting the output facet. Because of the tapered shape, even relatively low power light can trigger an avalanche of photons which is focused onto the narrow waveguide, possibly exceeding the maximum power density and leading to permanent damage. Typical sources of such damage are reflections, either from parts further down the setup or from an IR-card, which typically has a reflective surface as well. For this reason, an optical isolator is absolutely necessary, all lenses before the isolator should be placed at a slight angle of 2 - 3 ° [12].

During operation applying the correct voltage is also critical. To high voltage spikes or reversed voltage will lead to an electrical breakdown, destroying the chip. A protection circuit, which filters voltage spikes, limits over voltage and weakens reversed voltage is specified and characterized in section 3.3.1. The same damage can occur through electrostatic charge which can build up in the chip when it is not operated. While this is not a frequent problem, it has been observed to destroy the chip [12]. It is not absolutely necessary but safest to short both the anode and cathode when the TA is not operated.

When the chip is not seeded, but operated at high currents, thermal relaxation of electrons from the excited state will lead to excess heat which the cooling element might not be able to remove, leading to degradation and eventually destruction. This is most important, when the seed laser is blocked accidentally and without notice. An automatic current limiter, driven by a beam splitter and a light diode right before the TA as described in [12] can be used if this might be a problem. Conversely, seeding at high power without sufficient current leads to excessive heat and thermal degradation as well. Furthermore, in rare cases it has been observed [12] that seeding can destroy the chip in an instance, which is suspected to be caused by electrostatic charge resulting from photons exciting the ground state electrons. A precaution that can be met is to install a shutter in front of the laser that closes when no voltage is applied to the chip. Since the TA in this experiment is inside a closed box and expected to run through the whole experiment, we decided that there is no need for these precautions in our case.

Because the seed laser is acting as optical tweezers, dust particles in the air will be drawn and burned onto the facet. Moisture can be an additional source of degradation. The TA, therefore, must be inside a protective case. Dry silica can be placed inside the case if the laboratory environment is not sufficiently dry.

Table 2.1.: Overview of sources of permanent damage, possible precautions and their importance. [12]

Source	Precaution	Importance
Excess heat when soldering	Correct soldering	Critical
Damage to pumping wires	Careful setup	Critical
Light beam into output	Optical isolator at output	Critical
Reversed polarity	Protection circuit	Necessary
Voltage spikes	Protection circuit	Necessary
Dust	Protective case	Necessary
Moisture	Dry silica inside case	Optional
Electrostatic charge	Short + and - when not operated	Optional
High current without seed	Current limit when not seeding	Optional
Seeding without pumping	Automatic shutter	Optional

2.2. Reference Cavity

In order to excite a broader range of $\mathrm{H}^2\,\Sigma^+, \mathrm{H}'\,{}^2\Pi$ states, the last of the three lasers needs a variable locking system, preventing the laser from drifting and allowing to scan over a known frequency spectrum. A relative frequency reference is acquired using a Fabry-Pérot Interferometer [1]. A Fabry-Pérot Interferometer is an optical cavity consisting of two parallel, partially transmitting mirrors with the reflectance $\mathrm{R}_1$and R_2 as depicted in figure 2.5. Light enters the cavity, travels the distance L, is reflected at one of the mirrors and then travels back to the first mirror in the time Δt. As the reflection index of the mirrors is high and transmission index is low, light is usually reflected several times before transmission or absorption occurs. If the light arriving after one round trip is in phase with the light entering the cavity, that is if it can interfere constructively at the boundary, it has a finite possibility to be transmitted. Therefore, whether constructive interference occurs depends on the length of the cavity, the wavelength and the time it takes for the light to travel this distance. Light that arrives with a slight phase shift due to a different wavelength will interfere destructively and with every reflection the phase shift will increase. Due to the many reflections appearing, the range of frequencies at which constructive interference occurs is narrow. Any other light has much lower possibilities of transmitting through the reflective surface and hence escaping the cavity.

A frequency at which the cavity transmits light is called a mode, the distance between two such mode frequencies is referred to as the free spectral range

$$\mathrm{FSR} = \frac{c}{2nL} \overset{\text{in air}}{\approx} \frac{c}{2L} \tag{2.1}$$

and is often the most important specification of the cavity. It depends on the distance L between the two mirrors and the refractive index n of the medium which

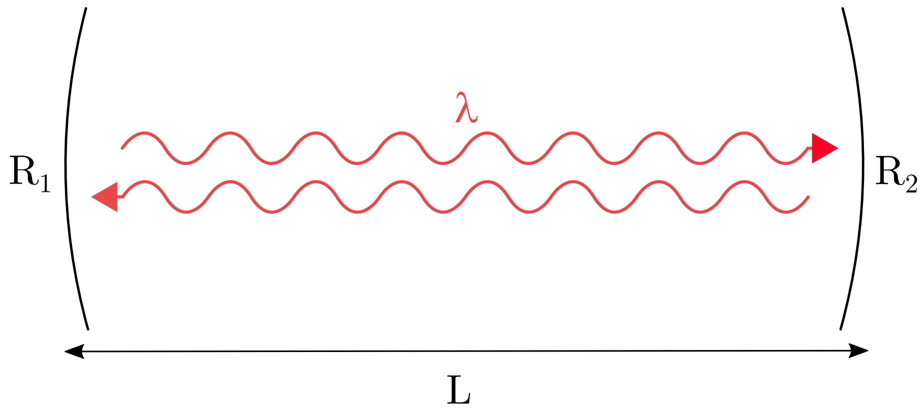

Figure 2.5.: Schematic drawing of a spherical resonator. The mirrors have the reflectance R_1 and R_2 and are the length L apart.

is approximated to 1 throughout this thesis because our cavity is filled with air. Another important specification of the cavity is the finesse F, which describes the cavities ability to resolve closely spaced spectral features. In theory the total finesse of the cavity is composed of the reciprocals of several factors, including the surface quality of the mirrors, beam alignment and diameter, and the mirror reflectance. In professionally assembled reference cavities, both the surface quality and reflectance is negligible, and the peak takes a Lorentzian form. The finesse can then be calculated as

$$F = \frac{\mathrm{FSR}}{\mathrm{FWHM}}. \tag{2.2}$$

Via a piezoelectric transducer the length of the cavity and therefore the FSR can be adjusted. Using a PID-controller, drifting of the cavity through thermal expansion can be eliminated and the frequency accurately set. This requires a stable locking laser, which is provided in the laboratory using a thermally isolated ultra low expansion (ULE) cavity. The FSR can then be adjusted, so that the stable light of the laser matches a mode and any change on the power meter behind the cavity leads to correction of the cavity length via the piezoelectric transducer.

3. Setup

This chapter describes the setup of the laser system and explains the necessary basics to realize it. We begin with an overview of the setup and continue to show how the seed laser has been shaped. Then we describe the setup of the tapered amplifier, including the protection circuit that has been build, the calibration of the diode controller and the coupling process. Unfortunately, the setup could not be completed in the time available because unexpected difficulties occurred during the TA setup (see section 3.3.7). We describe the sources of failure we have inspected, but were not able to definitively determine the problem. Finally, we mention the setup of the reference cavity.

3.1. Overview

The setup is placed on an optical table with room temperature of about 20 °C. The relevant parts and the beam trajectory are depicted in figure 3.1, the nomenclature of the figure and the focal lengths of the lenses are listed in table 3.1. During troubleshooting several lens combinations of L3 - L6 have been tested (see section 3.3.7) to no avail, hence we have listed the lenses which we suspect should work the best. The setup behind the TA has not been realized because it is impractical to do so when the TA is not working as expected.

Table 3.1.: List of relevant parts and important specifications and abbreviation used in figure 3.1. All lenses are B-coated. Lens L5 is optional.

PBS	2 Polarizing beam splitters	L1	Cylindrical EFL = 100 mm
$\lambda/2$	3 Half-wave plates	L2	Cylindrical EFL = 50 mm
OI	Optical Isolator	L3	Spherical EFL = 100 mm
TA	Tapered Amplifier	L4	Spherical EFL = 200 mm
DL	Diode Laser	(L5	Cylindrical EFL = 120 mm)
RC	Reference Cavity	L6	Aspherical EFL = 11 mm
		L7	Aspherical EFL = 4.51 mm
		L8	Unknown
		L9	Unknown

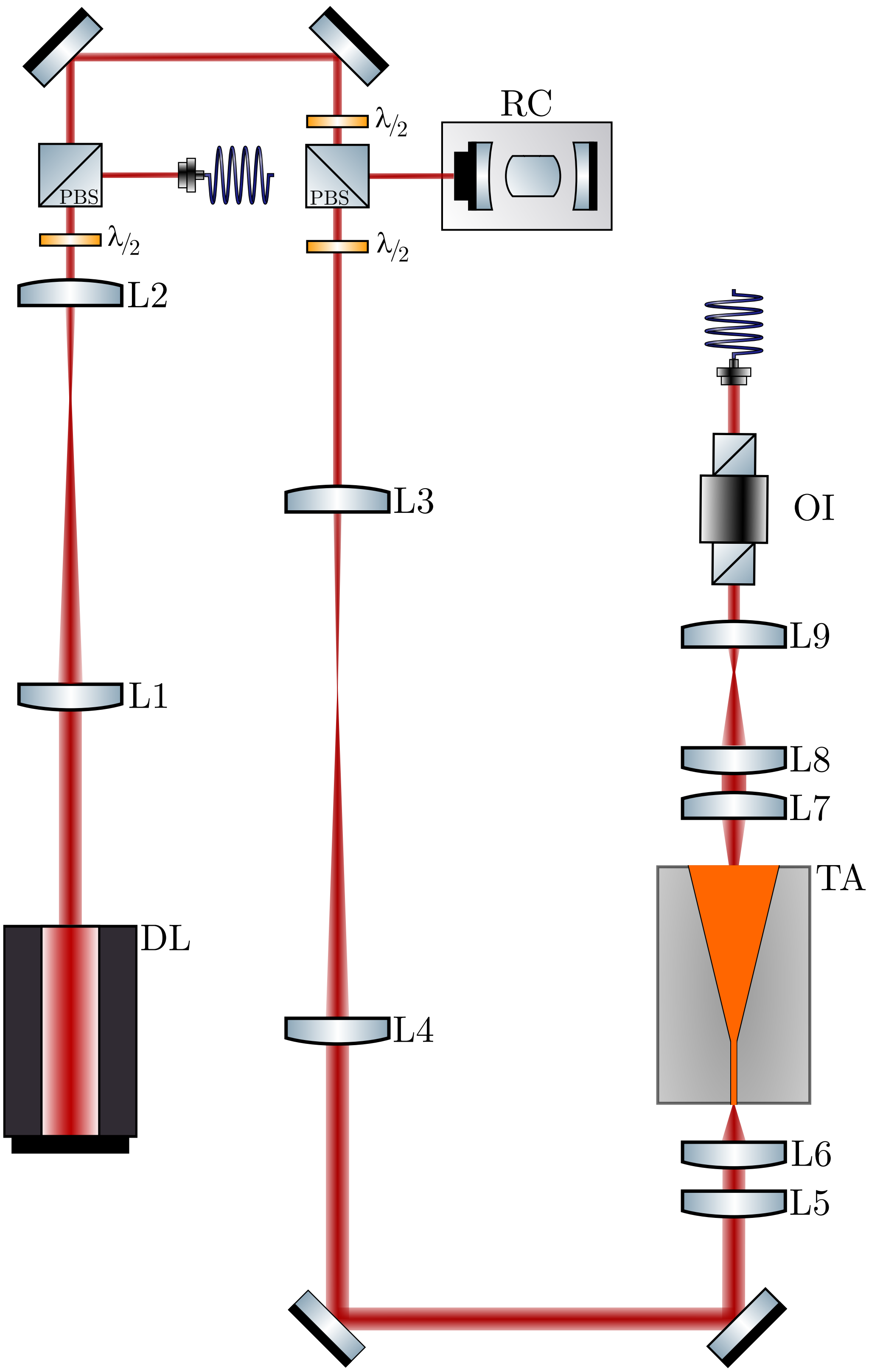

Figure 3.1.: Simplified laser setup designed during this thesis. Mirrors used for beam alignment are not depicted. The list of parts is given in table 3.1.

3.2. Seed Laser

For successful coupling, the seed laser and the ASE of the tapered amplifier must overlap as good as possible. The ASE of the tapered amplifier is highly divergent and astigmatic, which means that it has different rates of divergence in horizontal (x) and vertical (y) coordinates. For the coupling to be technically possible, first both beams must be collimated and brought into similar shapes and polarizations. The seed laser has been observed to emit an elliptic beam with a slight divergence in x direction. A pair of cylindrical lenses L1 and L2 form a telescope in the x direction for a more symmetrical and collimated beam. After this first shaping, assuming a Gaussian beam, the seed beam has a $1/e^2$ width of $w_x = 2\,\mathrm{mm}$ and $w_y = 2.6\,\mathrm{mm}$. However, as is seen in figure 3.2, it needs to be mentioned that the laser resembles a Gaussian beam only in y direction, while the center of the x direction is misplaced. This however should not have any effect on the function of the TA.

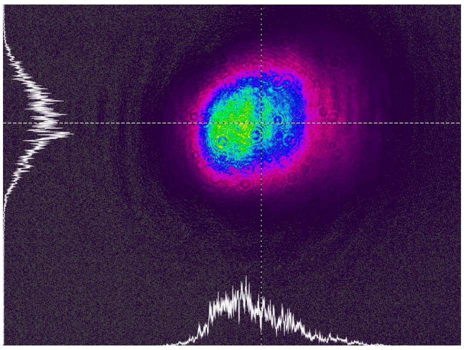

Figure 3.2.: Measurement of the collimated seed beam. Some optical distortions, which probably result from dust on the sensor or thermal damage, are visible.

After the beam shaping we can use two polarizing beam splitter cubes (PBS) and two $\lambda/2$-plates to branch off light into the reference cavity and a multi-mode fiber leading to a wave meter. Subsequently we collimate the ASE of the tapered amplifier using a cylindrical lens L5 and an aspherical lens L6.

3.3. Setup of the TA

In this chapter we will see how to set up the tapered amplifier. We begin with the construction and testing of a protection circuit. Then we show how to calibrate the controlling unit and calculate the necessary parts based on the chip dimensions. Then we look at the assembly and coupling of the tapered amplifier. In the end we also present a small troubleshooting guide from our gathered experience for the case that the amplifier does not work as expected.

3.3.1. Protection circuit

As a safety measurement against destruction, a protection circuit has been build after the schematic in figure 3.3 on the basis of an existing, older circuit, and has been improved by adding an additional diode to improve the reverse voltage drop and a 10 kΩ resistor to better protect the chip from voltage spikes. The circuit has then been characterized and its function confirmed by applying a 1 V noise signal (figure 3.5) and a 1 V rising edge (figure 3.6). In the characterization curve in figure 3.4 it is evident, that the circuit is not hindering the TA in its operating regime of 1.2 - 1.6 V, dampens dangerous voltage above 4 V and reduces reversed polarity voltage by roughly 50 %. Applying a noise signal smooths the signal out completely (figure (3.5)), but due to the damping effect on reversed polarity voltages, the output is slightly above 0 V. When the input voltage suddenly rises (figure (3.6)), the output rise time is delayed for about 1 ms. We can conclude that all features of the protection circuit work as expected.

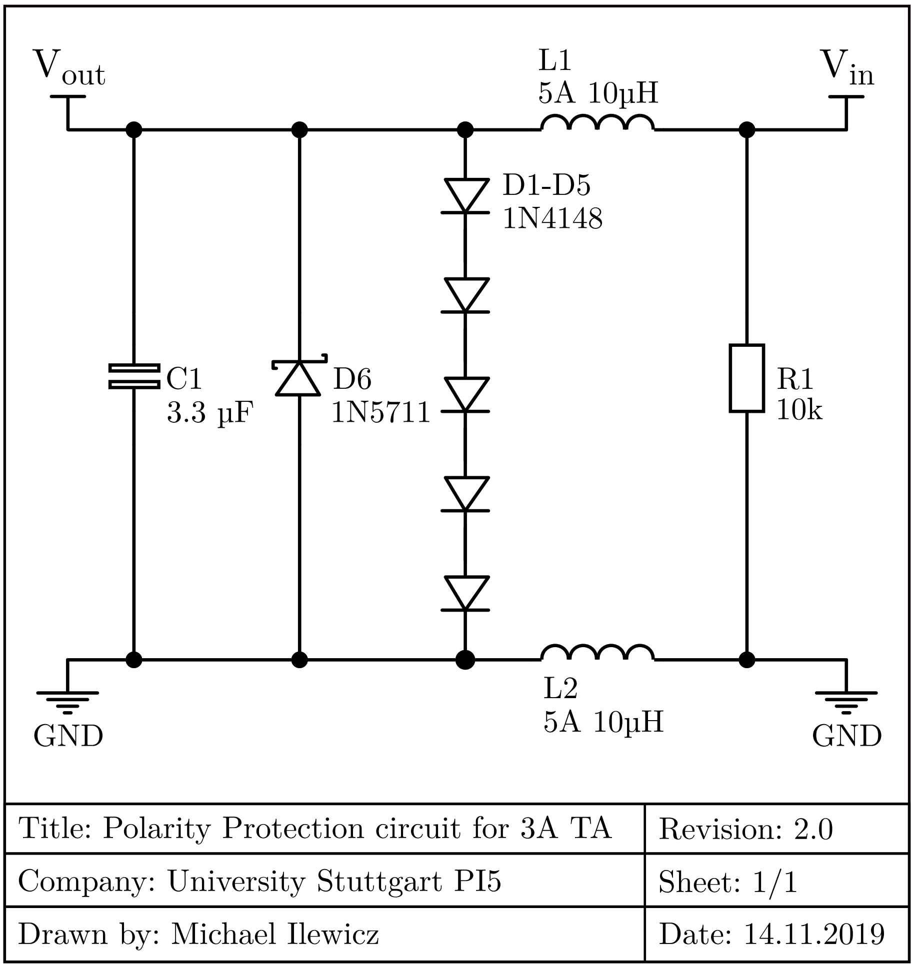

Figure 3.3.: Schematic of the polarity protection circuit used in this thesis.

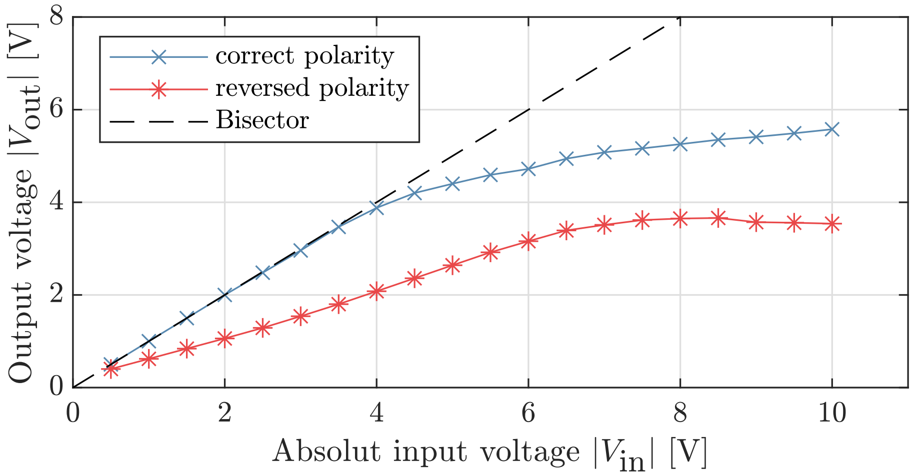

Figure 3.4.: Output voltage of the protection circuit in correct polarity and reversed polarity for different voltages. In comparison is the bisector visualizing where the output voltage without protection circuit would be.

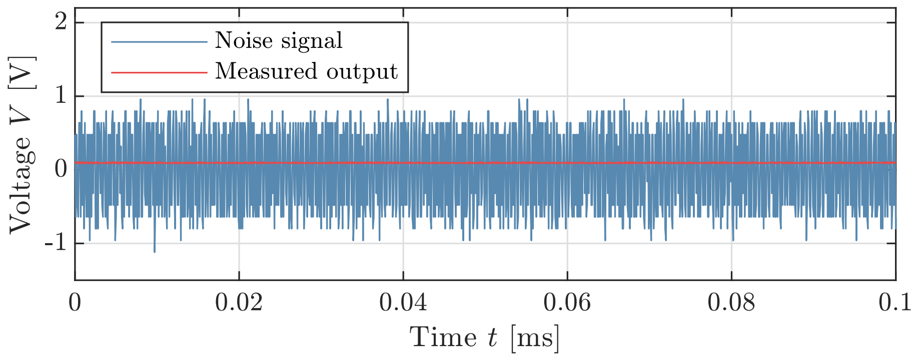

Figure 3.5.: Output of the protection circuit to a noise signal of 1 V.

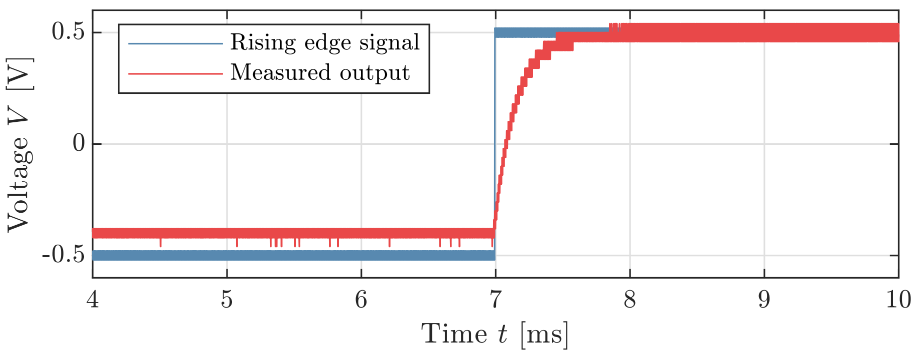

Figure 3.6.: Output of the protection circuit to a sudden voltage edge of 1 V.

3.3.2. TA-chip controller

The voltage, current and temperature of the TA is controlled using a Thorlabs ITC133 OEM laser diode controller [16] which can deliver up to 3 A and 18 W to the chip. The output power of the TA is regulated by adjusting the current. To protect the chip from degradation, it is possible to define the maximum current that will be needed in the experiment. Before the TA-chip can be implanted, the PID controller, responsible for the temperature regulation, as well as the internal readings of the controller must be calibrated. While the TA-chip controller manual [16] does provide an example of a PID adjustment, it has been experienced that it is of advantage to understand the basics of PID controlling for the calibration process. Therefore, a quick overview is given in the following.

PID Controller

The abbreviation PID stands for Proportional-Integral-Derivative [17]. This control approach is used for almost all systems in which the controlled process has a finite response time, such as for most temperature regulations. As described in the block diagram in figure 3.7 the controller calculates the difference between the set value and the actual value measured in the process and saves the result into the error function $e(t)$. The controller then calculates one control value P proportional to the error function, one control value I proportional to the integral of the error function over a certain time period, as well as one control value D proportional to the first derivative of the error function. The sum of those values is then used as the control value to drive the process. The weighting of the above system properties depends on the gain values $K_{P,I,D}$, an overview of the effects of each gain value is given in table 3.2.

Table 3.2.: Effects of adjusting individual PID gain values on the system. [17]

Parameter	Steady-state error	Speed	Stability
K_P	Reduces	Increases	Decreases
K_I	Eliminates	Reduces	Increases
K_D	No effect	Increases	Increases

Proportional controller This controller deals with the present error. Increasing the gain K_P will in general speed up the time response but, as the process responses delayed to any control value, and the proportionality action has no knowledge about future or past, this will also lead to instability. Additionally, if the error is small than the proportional action might become insignificant and a steady-state error occurs.

Integral controller This controller uses information about the past to eliminate the steady state error. The small offset is integrated over time, ultimately increasing the response until the integral action is making significant impact. However, as it is necessary for the error to occur for some time before impact is made, this action has a low response time.

Derivative controller Most important for damping oscillations is the derivative controller, which anticipates knowledge about the future, extrapolating the current pace of change. If the error decreases, this action is negative, hence having a dampening effect on the proportional controller and slowing the process change down. Conversely, when the error increases, the derivative controller increases the control value to reach a decrease in error sooner.

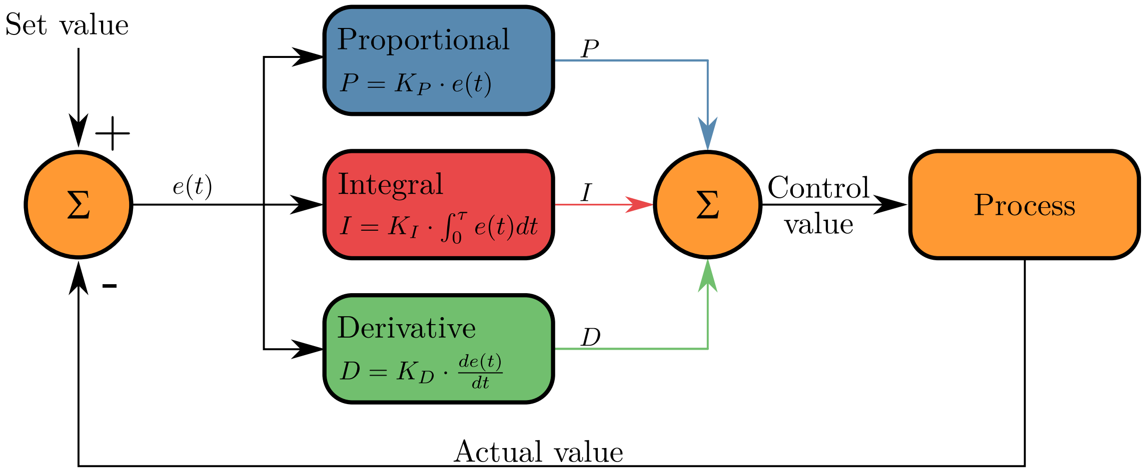

Figure 3.7.: Block diagram of the PID system control. The factors K_P, K_I, K_D have to be determined individually for each system through an empirical approach. Σ denotes the summation operator.

PID calibration

The control loop can be calibrated by adjusting potentiometers which set the gain values $K_{P,I,D}$. A simple strategy to approach the PID calibration is proposed in [16] and summarized here:

1. Completely setup the TA-system on the optical table, including the protective case but **not** the TA-chip.
2. Turn all PID Values to the minimal value.
3. For the following, change the set temperature between 18 °C and 22 °C after each step and observe the settling behavior of the temperature
   a) Adjust K_P in small steps until the temperature remains stable after 2-3 overshoots.
   b) Adjust K_D in small steps until the temperature has minimal overshoots.
   c) Adjust K_I in small steps until the temperature reaches the set temperature in shortest time without overshoots.

Internal reading calibration

Given that the used controller has been recycled from another project, recalibration needs to be done using the potentiometers P1 - P6 to ensure that the correct current is supplied even with the protection circuit attached. The detailed calibration process is described in [16], a short summary is presented here:

1. Put the protection circuit in place and connect a multimeter to its output.
2. Adjust the maximum current to the highest value and adjust the diode current to 90% of the maximum current. Adjust P2 until the reading of the controller and the multimeter are equal.
3. Adjust the maximum current to 90% of the highest value and adjust the diode current to the maximum value. Adjust P3 until the reading of the controller and the multimeter are equal.
4. Connect the multimeter to the Peltier output and adjust the cooling current limit to 90% of the maximum value. Set the temperature to a significantly higher value and adjust P6 until the maximum cooling current and the measured current are equal.
5. If using a thermistor, disconnect the thermistor, measure the resistance without touching it with your hands and reconnect it. Adjust P5 until the actual thermistor value is the same as the measured value.
6. Adjust the set temperature to 90% of its maximum value. Turn on the temperature control and let the temperature settle. Adjust P4 until the set temperature and the actual temperature are equal.

3.3.3. Calculation of necessary parts

In this chapter we give an example on how to calculate the necessary specifications of the parts needed to couple in and out of the laser.

Seed diameter and input lens

Using Gaussian beam simulators [18], we can determine what the seed beam diameter and input lens must be to achieve the necessary $3\,\mu$m beam waist at the focus point. With the given Parameters of $\lambda = 835\,\text{nm}$, we find that at our minimum beam diameter of $w_y = 2\,\text{mm}$ we can pick any lens with a focal length of less than 6 mm as input lens. A lens with a larger diameter allows for easier coupling, because the total angular spread of the laser is smaller and the lens position does not have to be as perfect. On the other hand, a larger beam diameter is needed when the focal length increases. This is limited by the clear aperture (CA) of the lens, which is the maximum diameter through which light can pass. For this TA design, a molded aspheric lens with an M9 thread is needed. At our supplier the possible lenses have a CA in the range of 4.5 - 5.5 mm. In the worst case scenario it is acceptable that only the $1/e^2$ diameter of the beam, which contains 86.5 % of the power, fits through the lens. Hence, the maximum focal length that can be used is 13 mm when the $1/e^2$ diameter of the seed beam is not greater than 4.5 mm. Our beam is larger in the horizontal direction with $w_x = 2.6$ mm. Using a 13 mm lens, we can include a 1:2 telescope for coupling with greatest simplicity. Since the clear aperture for lenses of this size is around 5.5 mm, the power trough the lens would be approximately 95 %.

Output shaping and optical isolator

In order to find the correct outcoupling lens, the minimal numerical aperture (NA) and the maximal effective focal length (EFL) must be calculated to fit the requirements for the rest of the setup. The main limiting factor is the optical isolator (compare to figure 3.8), included to prevent reflections from the setup further down which would definitively harm the TA. The first available isolator is the Thorlabs IO-5-850-VLP which has an input diameter of $d_{\text{in}} = 4.7$ mm. We require that at least 98 % of the amplified beam can pass through the isolator. Using another Gaussian beam calculator [19], we find that this is satisfied for $d_{\text{FWHM}} \approx 2$ mm. Furthermore, the maximal transmission power density of $P = 100\,\frac{\text{W}}{\text{cm}^2}$ must not be exceeded. The divergence angle at the FWHM value of the tapered amplifier θ_{FWHM} is 14 ° parallel and 28 ° perpendicular to its optical axis, the larger of those angles must be used for the calculation. The EFL can then be calculated to

$$\begin{aligned} \text{EFL}_{\text{max}} &= \frac{d_{\text{in}}}{2\tan\left(\frac{\theta_{\text{FWHM}}}{2}\right)} \qquad (3.1) \\ &= \frac{2\,\text{mm}}{2\tan\left(\frac{28^\circ}{2}\right)} = 4.01\,\text{mm}. \end{aligned}$$

However, a lens with such a short EFL can not be used for this TA design because the main piece is to thick. Since a cylindrical telescope has to be placed to collimate the stronger diverting axis of the TA, an alternative solution is to take a lens with a slightly bigger EFL but with the right NA and place a second telescope behind the TA to achieve the desired diameter. A good rule of thumb is to pick a lens with a numerical aperture of around twice the aperture of the light emitting entity

$$\text{NA}_{\text{TA}} = \sin(14^\circ) = 0.24, \qquad (3.2)$$

$$\text{NA}_{\text{Lens}} = 0.48. \qquad (3.3)$$

The lens with the most similar characteristics at our supplier Thorlabs is the A230TM-B with an NA $= 0.55 > 0.48$, a clear aperture CA $= 4.95 > d_{\text{in}} = 4.7$ mm and EFL $= 4.51$ mm. It is therefore our lens of choice.

Now we want to verify, that the maximum power density is not exceeded at any point. As a rough estimate, we assume that the highest power density is equally distributed in an area of half the FWHM area, or HWHM (half width half max) area, which certainly exceeds even the highest power density in the Gaussian beam profile. The power in this area can be calculated [19] to contain 15.84 % of the total power ($P_{\mathrm{TA,max}} = 1.1\,\mathrm{W}$). The area of peak power density is assumed to be

$$A_{\text{peak power}} = \frac{\pi}{4}\left(\frac{d_{\mathrm{FWHM}}}{2}\right)^2 = \pi\,(0.6925\,\mathrm{mm})^2 = 1.51\mathrm{mm}^2 \tag{3.4}$$

and hence the power density is in first approximation not much higher than

$$\frac{0.1742\,\mathrm{W}}{0.0151\,\mathrm{cm}^2} = 11.5\,\frac{\mathrm{W}}{\mathrm{cm}^2} \tag{3.5}$$

which is well below the threshold of $100\,\frac{\mathrm{W}}{\mathrm{cm}^2}$. The optical isolator can safely be used for this application.

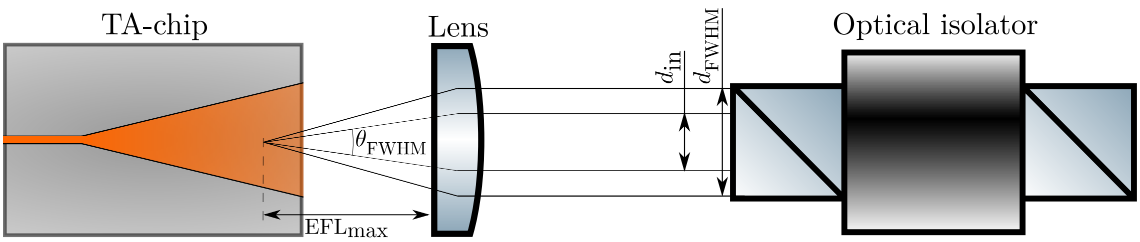

Figure 3.8.: Sketch of the important outcoupling elements and parameters of the TA.

3.3.4. TA-system assembly

The metal parts of the TA-system used in this thesis can be manufactured in any mechanical workshop. The corresponding plans can be found in appendix A. As seen in figure 3.9, the system consists of a chip mount, a heat sink and the protective cover. The chip mount is made of copper, is electrically isolated from the rest of the system (using nylon screws) and placed on top of a Peltier element which is used for temperature stabilization. It also contains a hole for a small thermistor close to the chip position, which is used to measure the case temperature. The chip mount holds two other pieces, the lens blocks, in which a tube with aspheric lenses is placed. The lens at the input size is used to focus the seed laser onto the waveguide, the output lens is used to collimate the highly divergent light emitted by the amplifier. Using precision setscrews (compare to figure 3.10), those lens blocks can be moved and rotated in every dimension which makes this design harder to set up than other designs but allows for good coupling quality and easy manufacturing.

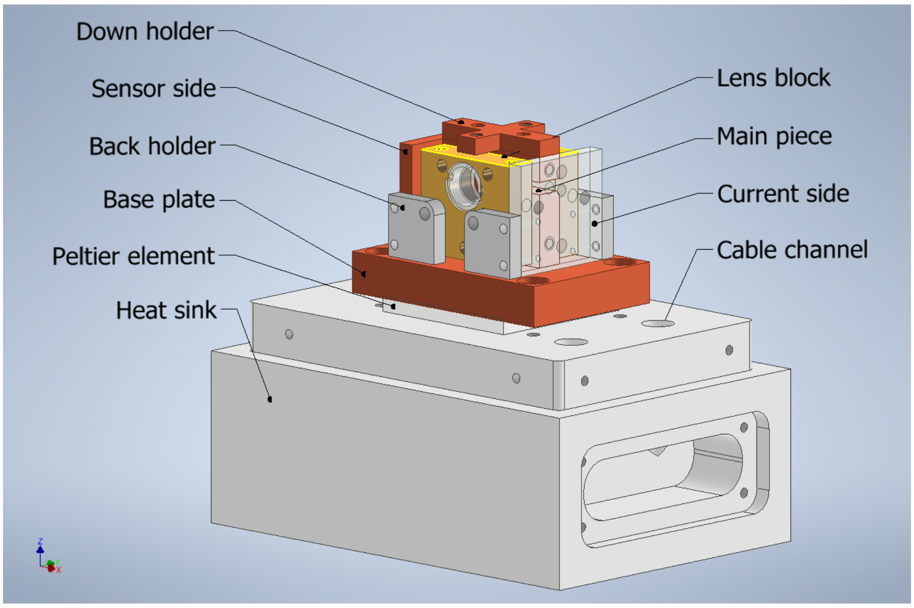

Figure 3.9.: Rendering of the complete TA-system after assembly without the protective cover and without screws. The current side piece is made transparent so that the main piece becomes visible.

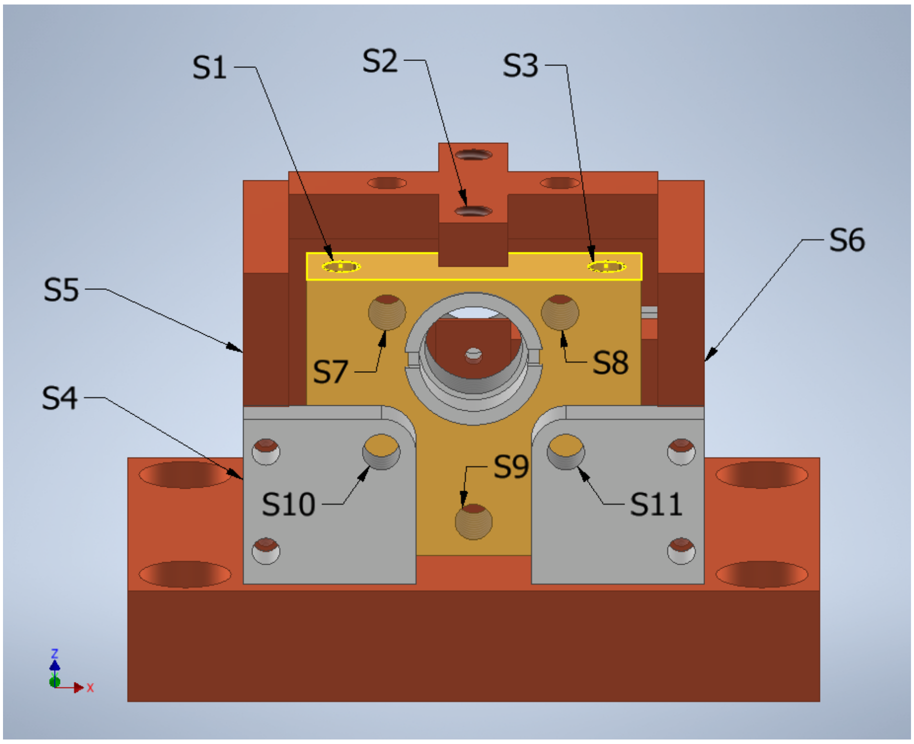

Figure 3.10.: Detailed rendering of the chip mount with annotations of the 11 setscrews used to calibrate the lens position.

The heat sink is made out of aluminum because it is easy to work with and has good heat conduction capabilities. A groove and two holes are made on the side so that the necessary wires are out of the way and do not disturb the cover.

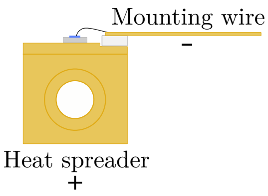

Figure 3.11.: Front view of the c-mount with the TA-chip on top of it.

As shown in figure 3.11 the TA-chip is placed on top of a c-mount, which acts as a thermal and electrical contact (in this case the cathode (+)) and is screwed onto the main piece. Before mounting the chip, a cable, thick enough to handle the maximum current of the chip, must be soldered onto the anode (−) and isolated from the chip mount using a shrink-tube. Then the chip must be put in place with extreme care, refer to chapter 2.1.2 for risks of improper handling. The chip used in this setup is specified in [20], table 3.3 gives an overview of the most important characteristics.

Table 3.3.: Most relevant specifications of the TA-chip used in this laser setup [20].

Characteristic	Value
Max. current	3 A
Max. output power	1.1 W
Center wavelength at 25 °C	830 nm
Amplification	13 dB
Divergence parallel (FWHM)	14 °
Divergence perpendicular (FWHM)	28 °

3.3.5. TA-coupling

As mentioned before, the design of this tapered amplifier has the advantage of high calibrational potential and easy manufacturing because of the full 6 degrees of freedom the lens mount can be moved in. However, this also makes first assembly difficult as the seed laser must hit the lens in its center to provide highest coupling efficiency. Inefficient coupling means that more light is dissipated into the not active parts of the chip, leading to increased thermal stress and therefore to a reduced lifetime. The first chip used in this setup was damaged, during troubleshooting frequent recalibration was needed. This led to the development of an algorithm for quick and proper setup of this specific TA design, which is now presented.

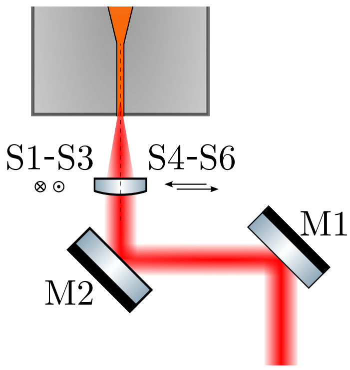

Figure 3.12.: Detailed view of the incoupling optics.

1. Place two mirrors anti parallel to each other as depicted in figure 3.12 and align them, so that the beam is reflected from M2 along a series of holes on the table and at exactly chip height (about 10 cm but depending on the Peltier element used). Make sure that the input power is within the limits of the chip, around 15 mW should be sufficient. Place a contracted iris far away from the TA, so that the maximum power is let through.

2. Insert the lenses into the lens tubes and make sure that they sit tight and do not move. Insert the lens tubes into the lens blocks, and use the setscrews to position the block straight and central. Make sure that the output lens block is slightly rotated (2 - 3 °) to avoid back reflections. Block the seed beam and place the TA in its place.

3. Run the TA at low current, do not exceed 1 A (or as specified). Collimate the ASE in the vertical direction on both sides of the chip by moving the lens tubes in or out. Use the setscrews (as denoted in figure 3.10) S1 - S3 and S4 - S6 to ensure that the ASE leaves the TA in a straight line, and check if it is still collimated.

4. For initial alignment of the beam iterate over the following two steps until there is no longer any need for change.

   a) Observe the ASE with an IR card as far as possible away from the chip[1] and turn mirror M2 so that the ASE and the seed beam overlap.

   b) Observe the ASE directly in front of the TA and turn M1 so that the seed beam is centered in respect to the ASE.

5. Open the iris, place a power meter at the output and see if the power changes when you turn the $\lambda/2$-plate. If you see a change in power, leave the plate in a position with maximum gain. If not, go back and look for possible mistakes (see chapter 3.3.6).

6. If you see a rise in output power, you are already seeding your tapered amplifier, you will, however, want to optimize the seeding further. Due to the small size of the facet, it is most important that the optical axis of the lens is exactly aligned with the waveguide of the chip. Adjust the position of the lens block by turning S1 - S3 in small steps and walking up the mirror in the vertical direction after each step until you reach a maximum. Repeat with S4 - S6 and the horizontal mirror alignment, and check whether the vertical direction is still optimized.

7. Adjust the lens position further by turning the screws S7 - S11 individually and try to maximize output power. After each step, try to optimize output power by walking up your coupling mirrors M1 and M2 until you find a position of highest power. Return to the previous position.

[1] If the ASE is so divergent in the horizontal plane that you can not observe the center of the ASE you can place a cylindrical lens into the beam before the mirrors (L5 in figure 3.1).

8. If you still experience low power, your facet might not be exactly in the beam focus. Start to turn the lens in or out in smallest steps or adjust S7 - S9 simultaneously.

3.3.6. TA troubleshooting

Since the TA-chip in this project has been found to be damaged, several possible sources of failure had been researched before checking the chip under a microscope. For future troubleshooting assistance, we summarize possible circumstances in this section, which can lead to unexpected behavior of the TA.

Polarity	If the seed power is at its maximum but the TA does not operate at its maximum yet, the polarity of the incoming light might be incorrect. Ensure linear polarity and place a $\lambda/2$-plate just before the TA input. Rotate it until the output power peaks.
Input current	Ensure, that even with the polarity protection circuit installed the electrical current set in the control unit arrives fully at the laser diode.
Input voltage	Ensure, that the voltage delivered from the control unit is within the specified limits and has the right polarity.
Large seed waist	The power of the TA is highly susceptible to correct lens focus. Ensure, that the seed beam diameter and the minimal beam waist is of the right dimensions. See chapter 3.3.3 for a calculation example.
Bad seed shape	The shape of the seed laser should be the same as the shape of the input ASE after collimation. Try to improve the shape of the seed laser.
Unsuitable lens	Ensure, that the lens is aspheric, has the correct coating and is clean. To make coupling less difficult choose a lens with the longest focal length at which your waist can still be small enough.
Damaged chip	Place the chip under a microscope and see whether any damage can be seen. Also make sure, that the pumping wires have not been bent.

3.3.7. Status quo

Unfortunately, even after investigating all the above aspects, It was not possible to set up the TA. While the first attempt did not succeed because the chip was damaged, we confirmed that the new chip has no visible damage on the facets. After all above troubleshooting attempts failed, we began to think of less likely circumstances that might lead to those difficulties, and experimented with the case temperature, checked that the seed laser is still emitting the correct wavelength and tried different approaches to the coupling process than the one described in section 3.3.5. Other people who did set up TAs with the same design before were also unsuccessful in locating the problem.

One possible problem might be that the coupling approach in its current form does not calibrate the lens position well enough.A good way of identifying the correct position of the lens block other than the output must be found. One observation that might lead to such a way is that turning in the lens tube causes the ASE to rotate. This might be caused either by wrong positioning of the lens or by an asymmetry. It has been tried to minimize this behavior, but as this idea was developed towards the very end of this thesis, a minimization of this rotation has not yet been observed. Further investigation is necessary. Should this hypothesis turn out to be true, steps 7 and 8 of the approach described in section 3.3.5 would have to be eliminated and after step 3 the following iteration would have to be included:

1. Rotate the lens tube and observe the ASE. When the block is in the right position in one of the dimensions, the ASE should not move in this dimension under rotation.
2. Using the setscrews, adjust the position in one direction. Continue with 1.

Since the position of the block could be critical to the micrometer, this iteration is extremely tedious. The setscrews must sit tight and be turned in small steps, alternating between screwing the setscrew(s) on one side in and on the other out. It is highly recommended to find a tool that makes turning the lens as easy as possible.

Setting up the optics at the output of the TA is impractical at this stage and will have to be done by another person once the TA is finally amplifying.

3.4. Reference cavity

For cost effectiveness, a custom made cavity after the design of [1], showed in figure 3.13, has been assembled by hand. As can be seen in figure 3.14, the peaks seem not to follow the Lorentzian peak form, but a non symmetrical form. One possible explanation for this is that the reciprocal factors mentioned in 2.2 are not negligible for this design and process of assembly. An alternative explanation may result from the limited capabilities of the used oscilloscope. Either way, as the knowledge of the finesse is not crucial for this experiment and other coworkers failed at determining the finesse of this custom design, this effect is not investigated any further. The set up is straight forward and simply requires two coupling mirrors and a photo diode at the output.

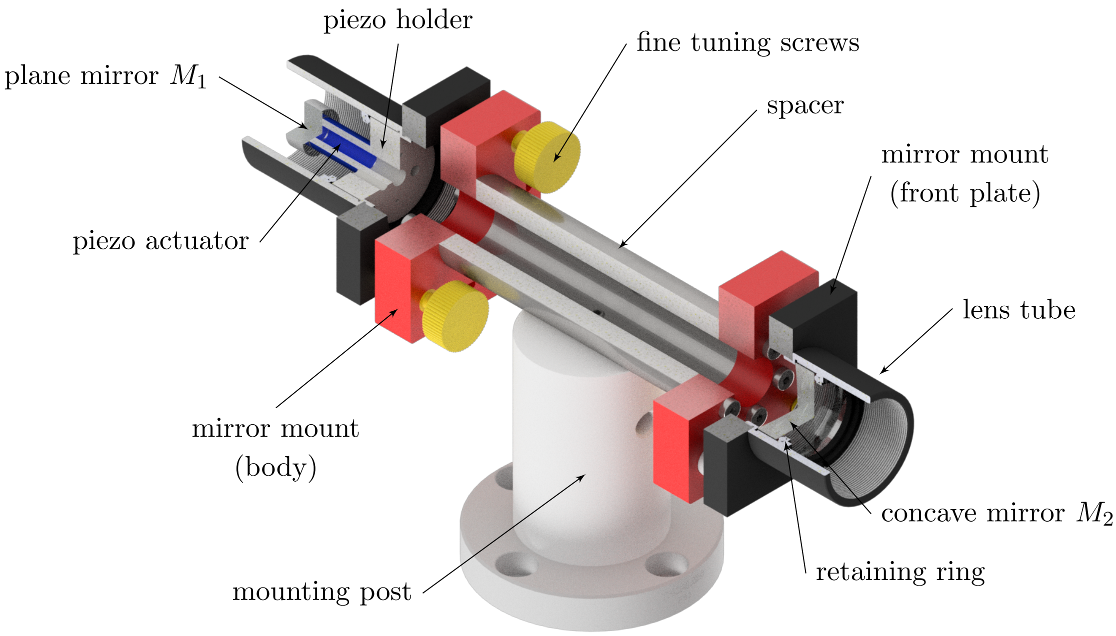

Figure 3.13.: Schematic depiction of the Fabry-Pérot interferometer design used in this setup [1].

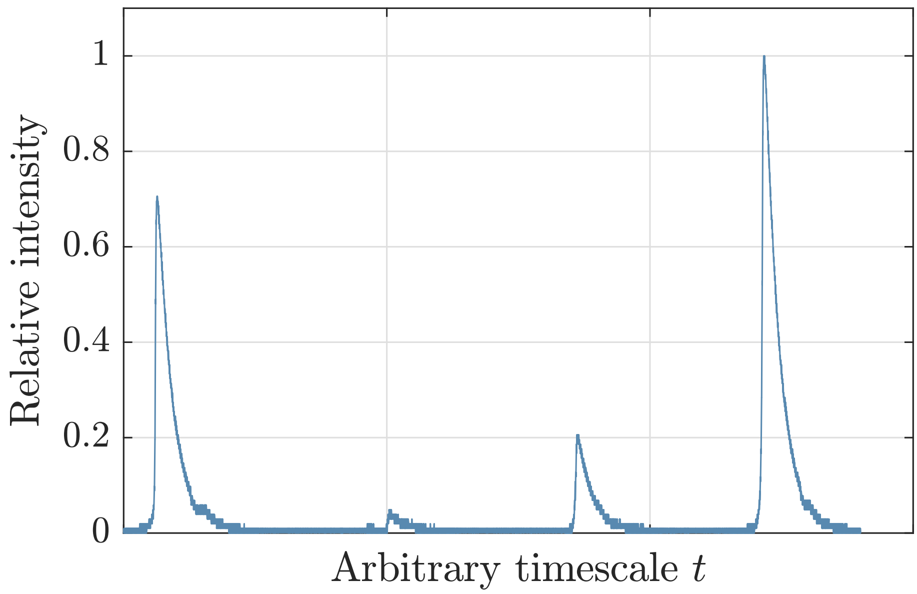

Figure 3.14.: Two main peaks and two side peaks of the custom made cavity. It is visible, that the peaks do not show a Lorentzian peak form, but have a decaying nature.

4. Characterization

After it was not possible to characterize the TA built for this thesis (see section 3.3.7), another TA of a neighboring project has been characterized for educational purposes and as a reference for future characterizations. This TA runs at 780 nm and can be operated with up to 3 A.

4.1. Tapered Amplifier

To increase the lifetime of the TA and to achieve maximum output power, it is necessary to know its characteristics. We are especially interested in the behavior at different pumping currents and seeding powers so that we know at which conditions we should operate the TA to achieve the highest gain and the most gentle operating conditions. In figure 4.1 the measured power is depicted in dependence of the pumping current for different seeding power. We can observe that for $I < 1\,\mathrm{A}$ the TA power rises harmonically and for $I > 1\,\mathrm{A}$ a saturation takes place and the power rises approximately linearly. We call this regime the pump saturation regime in which fluctuations are minimized [21]. In figure 4.2 the measured output power is shown in dependence of the seed power at pumping currents of 500 mA, 1000 mA and 1500 mA. We observe that at 500 mA the relation is different to the other two currents. We will investigate this further after calculating the gain. Additionally, we observe that there is another saturation effect taking place at seeding power $< 20\,\mathrm{mW}$ because the power is already increasing almost linearly. It would be interesting to observe the dependency for lower seed power, however, insufficient seeding at currents of 1 A and higher can damage the chip. Therefore, we limited the minimal seed power to 20 mW for this characterization.

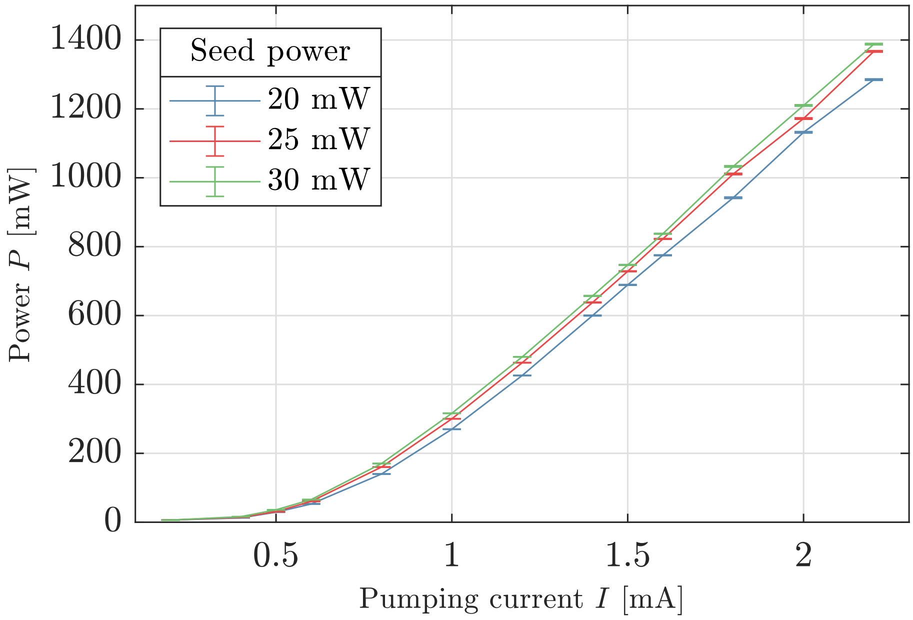

Figure 4.1.: Measured TA output power over the pumping current for three different seeding powers. As expected, higher seeding power yields higher output power.

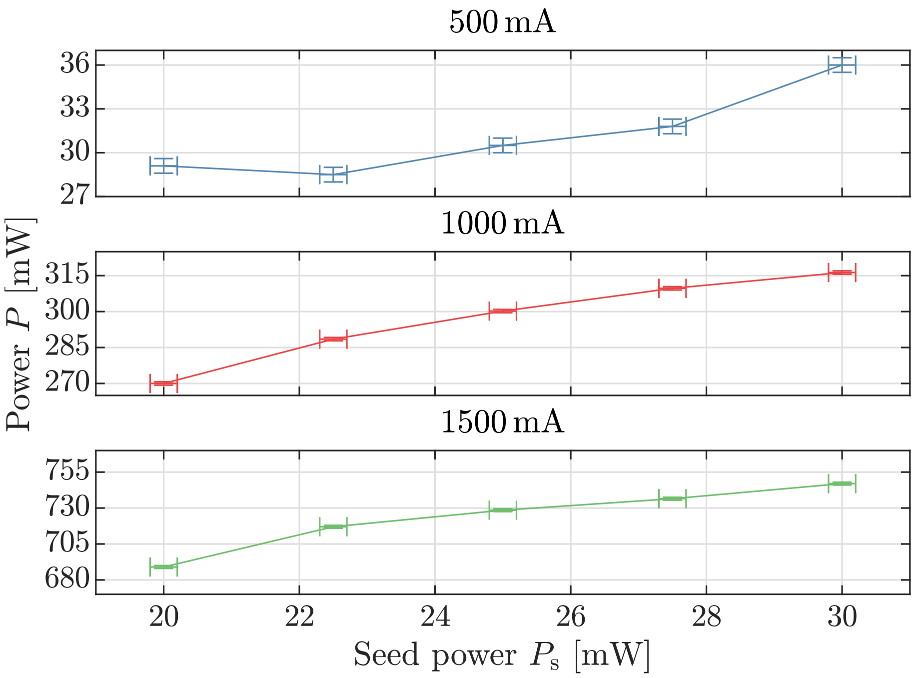

Figure 4.2.: Measured TA output power over seeding power for three different pumping currents.

The gain of an amplifier is a quantity that describes the increase in power. It is defined [22] as

$$G = 10 \cdot \log\left(\frac{P_{\text{out}}}{P_{\text{seed}}}\right) \tag{4.1}$$

and the error can be derived to be

$$\Delta G = 10 \cdot \sqrt{\left|\frac{\Delta P_{\text{out}}}{P_{\text{out}}}\right|^2 + \left|\frac{\Delta P_{\text{seed}}}{P_{\text{seed}}}\right|^2}. \tag{4.2}$$

During the measurement the seed variance has been estimated to be roughly $\Delta P_{\text{seed}} = 0.2\,\text{mW}$. The output power variance results from the thermal power meter used for the high power which needs some time to reach an equilibrium. this was estimated for each measurement individually by observing the fluctuations of the signal over roughly 30 seconds. We can calculate the gain with equation (4.1), the results are shown in figure 4.3 and 4.4. In figure 4.3 we see the saturation at 1 A more clearly. The TA begins amplifying ($G > 0$) at around 0.5 A which might explain the unexpected behavior for different seed powers at this pumping current. In figure 4.4 we see that the gain decreases with higher pumping power which means that the TA is already saturated in this regime.

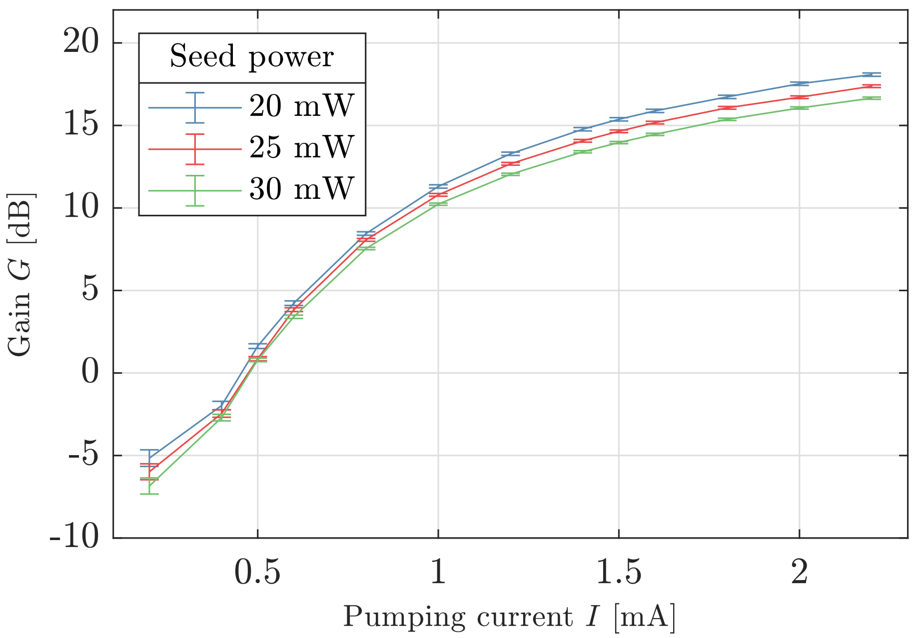

Figure 4.3.: TA gain over pumping current for different seeding powers. At 0.5 mA the TA just started to amplify.

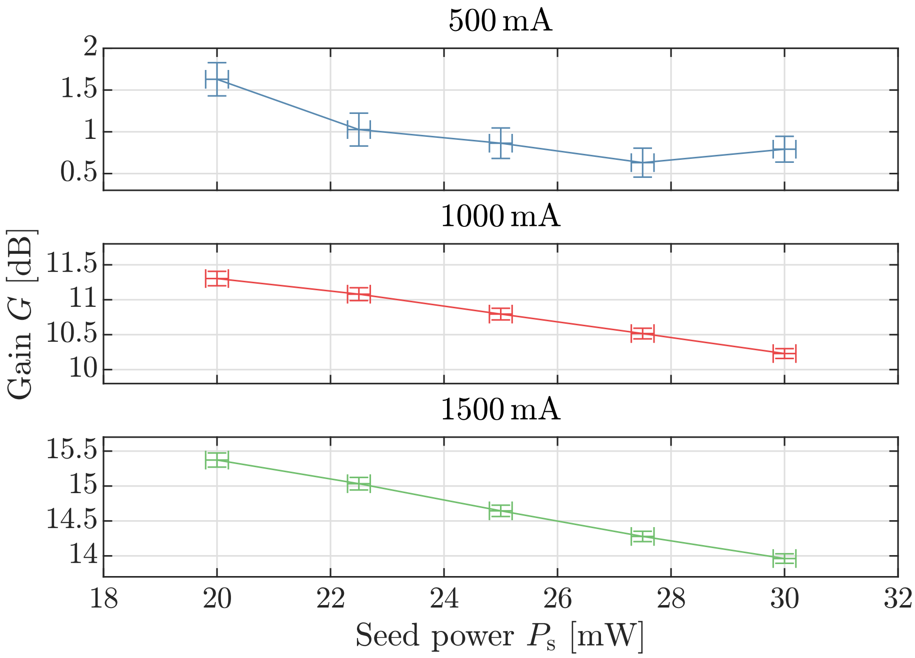

Figure 4.4.: TA gain over seeding power for different pumping currents. The gain decreases with higher seeding powers except for 500 mA pumping as this is the border where the TA begins to amplify, and irregularities occur.

It is also interesting to see how the output power depends on the light polarity. By rotating the last $\lambda/2$-plate before the TA, we can observe this behavior. Because operating the TA-chip with the wrong seed polarity is creating a lot of thermal stress in the chip, we only measure the polarization dependence at maximum 1000 mA and with a low seeding power of 10 mW. In figure 4.5a the normalized output power for the different positions of the $\lambda/2$-plate is shown. We can see, that the power at the minima is not 0 which is obviously caused by the ASE. We subtract the minimum, normalize the signal and calculate the average over the four polar quadrant intervals which yields a curve as shown in 4.5b. Here we can observe, that for higher currents the relative power is a little less dependent on the right polarization.

We are currently not aware of an explanation of this behavior in TA literature. However, we can think of one possible explanation by considering seeding saturation effects. The measurement is done at low seeding of 10 mW. Light with a shifted polarization has a component in the correct direction which is seeding the TA, and one component that is absorbed and heats up the chip. This means that the effective seeding power is even lower than 10 mW. In this region we expect that seeding does not fully saturate the TA-chip [23]. A smaller pumping current would mean that the population inversion decreases. When the upper state of the two level model (see section 2.1.1) is less populated, seeding saturation should set in earlier, which would explain the observed dependency.

The amplifier should be operated within saturation and with optimal polarization to

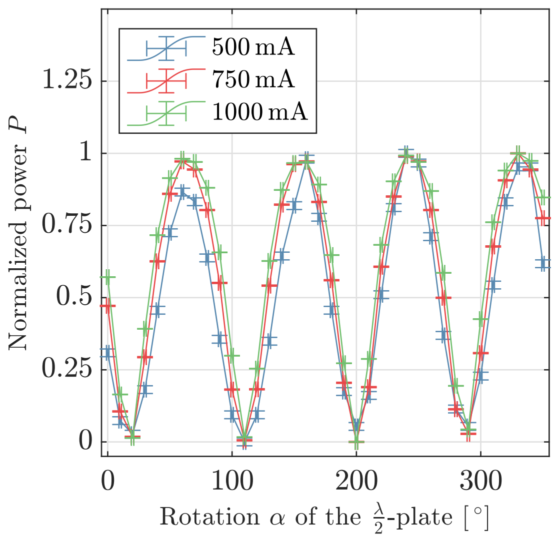

(a) Measured power. The ASE is not removed and responsible for the significant minimal power.

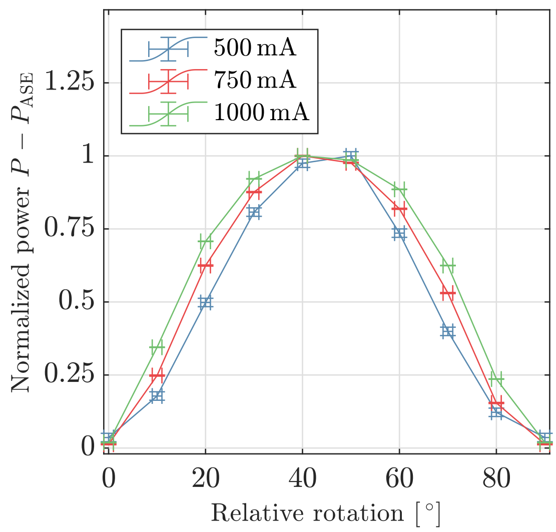

(b) Normalized output power for different pumping currents subtracted by the ASE and averaged over the four 90° quadrants.

Figure 4.5.: Observation of the normalized TA power in dependence of the seed laser polarization, controlled by the tilt angle α of a $\lambda/2$-plate in front of the TA, for different pumping currents.

maximize its lifespan. We can conclude that the TA should be operated at pumping currents of 1 A or higher and with 20 mW of seed power.

4.2. Reference Cavity

In order to have a frequency reference for the TA and the rest of the setup, building and characterizing a reference cavity is an additional part of this thesis. The cavity is designed to have a length $L = 160\,\mathrm{mm}$ but due to inaccuracies in the manufacturing of the individual pieces slight variation can occur. We assume an error of $\Delta L = 1\,\mathrm{mm}$. The theoretical value of the FSR can be calculated to

$$\mathrm{FSR} = \frac{c}{2L} = \frac{299\,792\,458\,\frac{\mathrm{m}}{\mathrm{s}}}{2 \cdot 0.160\,\mathrm{m}} = 937.5\,\mathrm{MHz} \tag{4.3}$$

with an uncertainty of

$$\Delta\mathrm{FSR} = \frac{c}{4L^2}\Delta L = \frac{299\,792\,458\,\frac{\mathrm{m}}{\mathrm{s}}}{4 \cdot (0.160\,\mathrm{m})^2} \cdot 10^{-3}\,\mathrm{m} \approx 3\,\mathrm{MHz}. \tag{4.4}$$

However, we want to verify this theoretical value. The FSR can be measured by varying the frequency of a laser which is coupled into the cavity and observing the output with a photodiode.

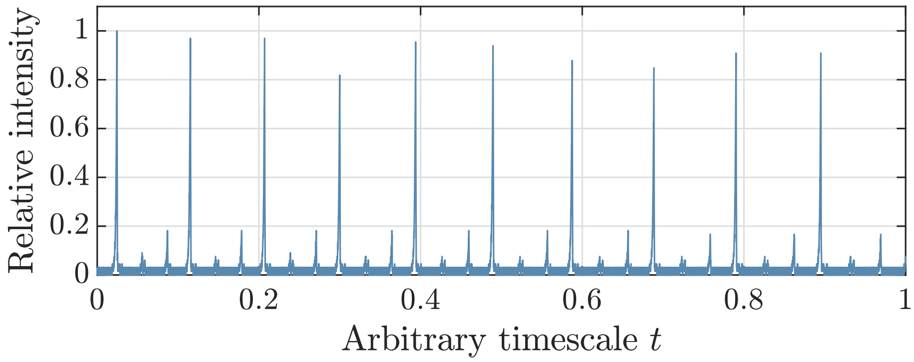

Figure 4.6.: Light intensity detected using a photodiode after the cavity. The input laser is scanning over a frequency band of roughly 10 GHz. Two secondary modes are visible, but the main modes are clearly distinguishable. The scan direction can be identified through the symmetry of the secondary modes

4.2.1. Spectroscopy mapping

The cavity has been coupled into a ^{87}Rb spectroscopy setup for characterization. This setup is scanning a frequency band of roughly 10 GHz at an unknown timescale, which we will arbitrarily normalize in the following. As shown in figure 4.6 this results in peaks in power which we identify as the longitudinal modes of the cavity. The rubidium spectrum is recorded at the same timescale as the cavity modes. By identifying known peaks within the rubidium spectrum, and calculating their transition frequencies, we can calculate the current frequency for each point on the arbitrary timescale and hence know at which frequencies the cavity has resonating modes. To increase the accuracy we choose two peaks with good clarity and greatest distance. We refer to those two transitions as

$$T_1 \equiv 5\mathrm{S}_{1/2}, F = 2 \to 5\mathrm{P}_{3/2}, F = 2\,\mathrm{co.}\,3, \tag{4.5}$$
$$T_2 \equiv 5\mathrm{S}_{1/2}, F = 1 \to 5\mathrm{P}_{3/2}, F = 1\,\mathrm{co.}\,2 \tag{4.6}$$

and their positions in our arbitrary timescale

$$t_{T_1} = 0.1485, \tag{4.7}$$
$$t_{T_2} = 0.8330. \tag{4.8}$$

The notation $2\,\mathrm{co.}\,3$ implies a crossover line and not a real transition which is the result of moving atoms reacting in resonance to the pump and probe beams with two separate transitions [24]. The difference in frequency between state 2 and 3 has to be divided by 2 to calculate the hypothetical frequency of this crossover line. The hyperfine structure frequencies for the D2 line of rubidium have been measured by [25, 26] and are illustrated in figure 4.7.

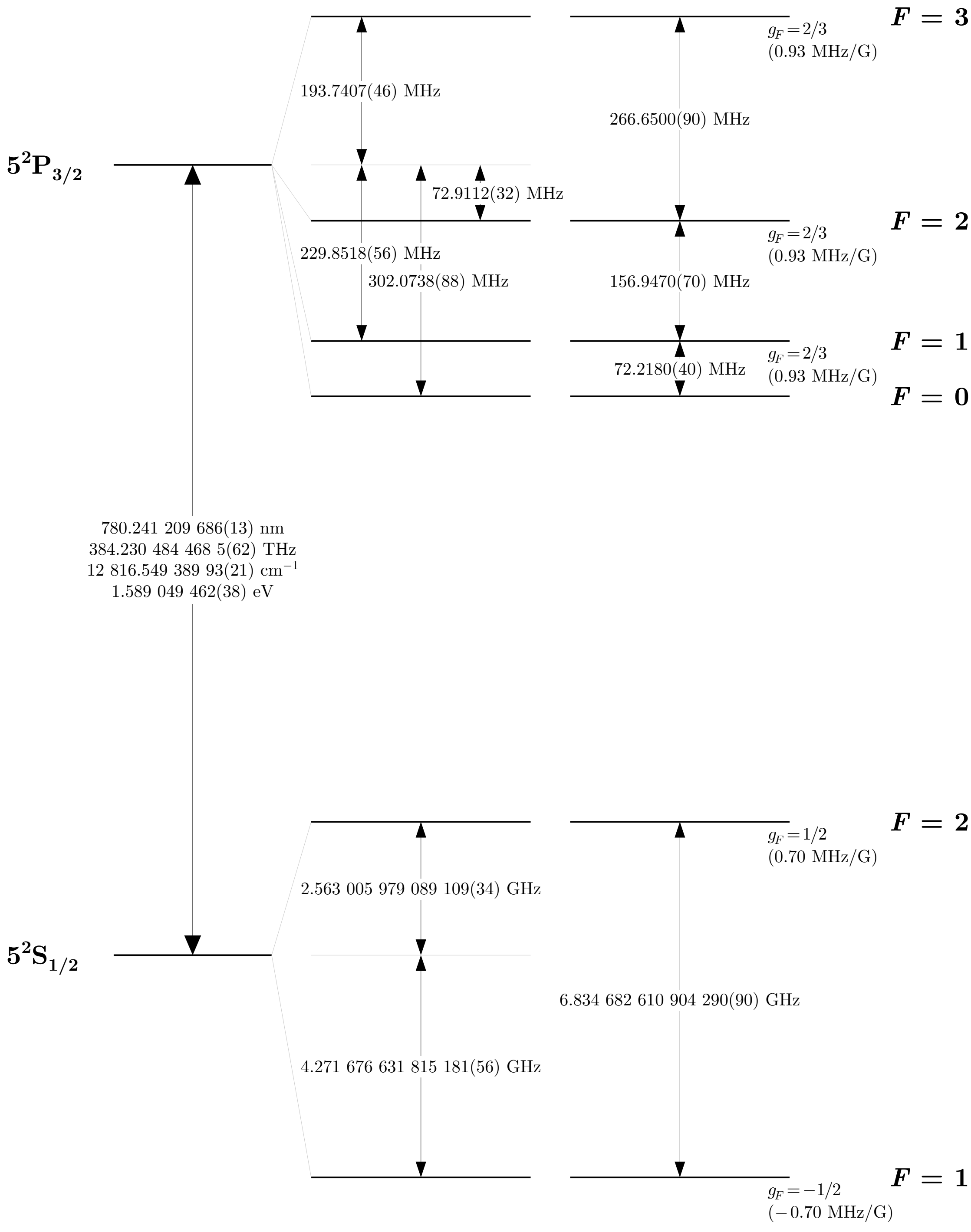

Figure 4.7.: ^{87}Rb D2 transition hyperfine structure, with frequency splittings between the hyperfine energy levels. [27]

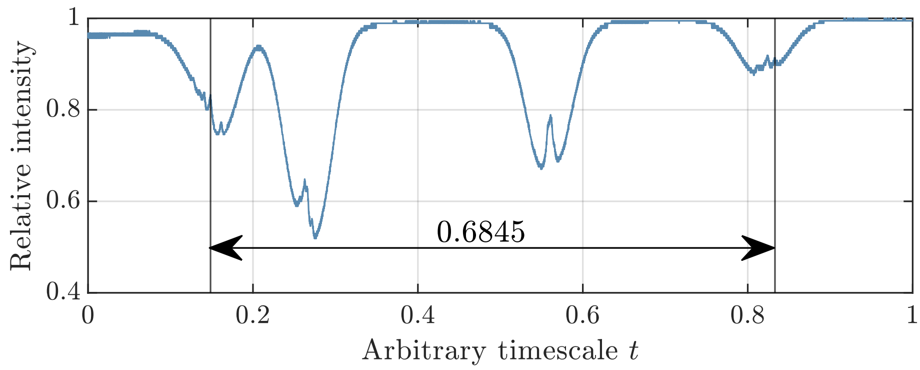

Figure 4.8.: Spectrum of the D2-line absorption of ^{87}Rb with location of the T_1 absorption peak at $t_{T_1} = 0.1485$ and the T_2 peak at $t_{T_2} = 0.8330$ in the arbitrary timescale of the scanning laser.

Using this data we can calculate the transition frequencies

$$\begin{aligned}
f_{T_1} &= 384230.4844685(62)\text{ GHz} - 2.563005979089109(34)\text{ GHz} \\
&\quad - 0.0729112(32)\text{GHz} + \frac{0.2666500(90)}{2}\text{ GHz} \\
&= 384227.981876(14)\text{ GHz}, \qquad (4.9) \\
f_{T_2} &= 384230.4844685(62)\text{ GHz} + 4.271676631815181(56)\text{ GHz} \\
&\quad - 0.0729112(32)\text{GHz} - \frac{0.1569470(70)}{2}\text{ GHz} \\
&= 384234.604760(13)\text{ GHz}. \qquad (4.10)
\end{aligned}$$

As these values are extremely well known, we want to neglect the uncertainties of the transition frequencies in this thesis. Assuming that the laser is scanning the band linearly, we can assign each point on the timescale in figure 4.8 to a corresponding frequency with the function

$$\begin{aligned}
f(t) &= \frac{f_{T_2} - f_{T_1}}{t_{T_2} - t_{T_1}}(t - t_{T_1}) + f_{T_1} \qquad (4.11) \\
&= \frac{384234.604760\text{ GHz} - 384227.981876\text{ GHz}}{0.8330 - 0.1485}(t - 0.1485) \qquad (4.12) \\
&\quad + 384227.981876\text{ GHz} \qquad (4.13) \\
&= 9.675506\text{ GHz}\,(t - 0.1485) + 384227.981876\text{ GHz}.
\end{aligned}$$

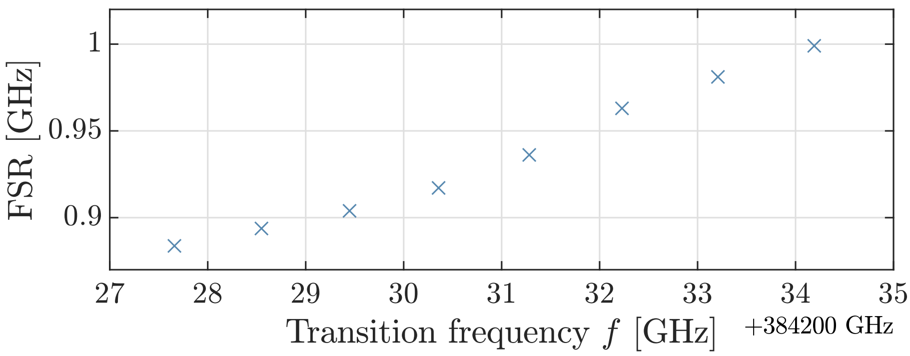

Figure 4.9.: The FSR calculated as the mean distance to the neighboring cavity peak.

We calculate the FSR as the mean value of the distances of two neighboring modes and, as can be seen in figure 4.9, we find that the FSR is not distributed linearly along the calculated frequency scale. This means that our initial assumption of a linearly scanning laser is inappropriate. The naive method to resolve this issue is to calculate the mean value of all FSRs which leads to

$$\mathrm{FSR} = 935\,\mathrm{MHz}$$

and a standard deviation of 43 MHz which is within the expected region. This deviation is to large for our needs. Therefore, we want to find another method with which we can calculate the FSR.

4.2.2. Non-linearity examination

A better approach is to compare the signal (see figure 4.10) of the cavity with an ultra low expansion (ULE) cavity which has a known $\mathrm{FSR}_{\mathrm{ULE}}$ of about 1.5 GHz but unknown certainty and is available in the same setup. Using the information, that in the frequency space all peaks must be linearly distributed, we can model a nonlinear timescale using a polynomial and fit the linear frequency space directly to the nonlinear arbitrary timescale. We define an array [12]

$$f_{\mathrm{ULE}} = \begin{pmatrix} 1.5\,\mathrm{GHz} & 3.0\,\mathrm{GHz} & 4.5\,\mathrm{GHz} & ... \end{pmatrix} \tag{4.14}$$

of points at which we expect the cavities to be located in the frequency space and an array

$$t_{\mathrm{modes}} = \begin{pmatrix} t_1 & t_2 & t_3 & ... \end{pmatrix} \tag{4.15}$$

which holds the mode locations in the arbitrary nonlinear timescale. We find that polynomials with grade greater than 4 do not yield any changes of value or standard

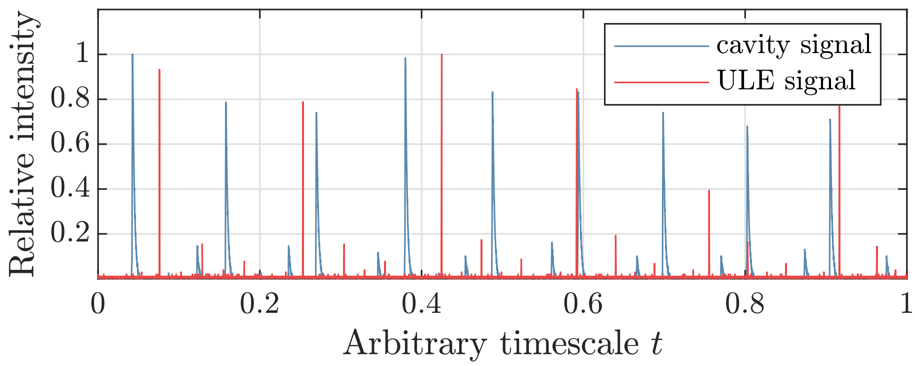

Figure 4.10.: Measured cavity modes and ULE cavity modes on the same arbitrary timescale.

deviation. We therefore model the frequency-time-dependencies of the scanning laser with

$$f = c_4 t^4 + c_3 t^3 + c_2 t^2 + c_1 t + c_0 \tag{4.16}$$

and use it to map our array t_{modes} to f_{ULE}. Hereupon, we use the calculated factors c_i to calculate a new frequencyscale in which we again locate the modes and calculate the FSR. This produces a result of $\mathrm{FSR_{cavity}} = 953(1)\,\mathrm{MHz}$. A Matlab™ function of this algorithm is given in appendix C. However, this result is already outside of the theoretical range of $\mathrm{FSR_{cavity}} = 937(3)\,\mathrm{MHz}$. Using equation (4.3) we can reconstruct the cavity length to $L = 156.5\,\mathrm{mm}$ which is $3.5\,\mathrm{mm}$ smaller than the designed cavity. The reason for this is that the exact FSR of the ULE cavity acts as a scaling factor for the new linearized frequencyscale. Repeating this calculation for $\mathrm{FSR_{ULE}} = 1.48\,\mathrm{GHz}$ results in $\mathrm{FSR_{cavity}} = 946(1)\,\mathrm{MHz}$ and for $\mathrm{FSR_{ULE}} = 1.52\,\mathrm{GHz}$ in $\mathrm{FSR_{cavity}} = 971(1)\,\mathrm{MHz}$. A third approach has been developed which combines the certainty of the rubidium spectroscopy with the linearity of the ULE approach but is not dependent on the FSR of the ULE cavity.

4.2.3. Rubidium spectroscopy with non-linearity correction

We can take advantage of the arbitrary nature of our timescale and the fact that we know certain points that should be distributed linearly. Instead of transforming directly into the frequency space we first create another arbitrary but now linear timescale $\tau(t)$. In complete analogy to the last approach we model the linear timescale with

$$\tau = c_4 t^4 + c_3 t^3 + c_2 t^2 + c_1 t + c_0 \tag{4.17}$$

but now define an arbitrarily array with equal increments

$$\tau_{\mathrm{modes}} = \begin{pmatrix} 1 & 2 & \dots \end{pmatrix} \tag{4.18}$$

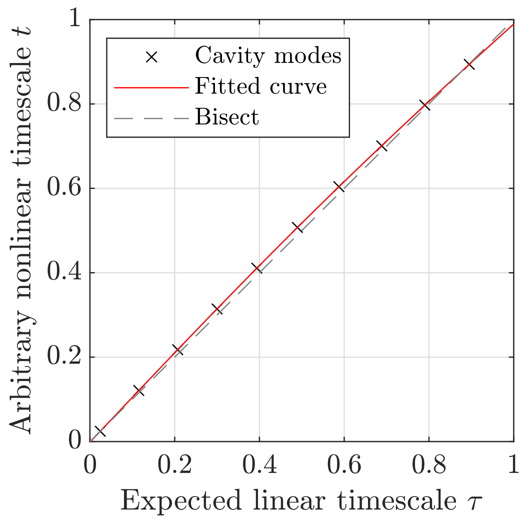

Figure 4.11.: Polynomial relationship between the non-linear timescale t and the linearized timescale τ.

which will correspond to the mode positions in the new linear timescale after normalization. Then we transform the measurement of the rubidium spectrum into this new timescale. The relationship of the two timescales is shown in figure 4.11. A Matlab™ function for this transformation is given in appendix C. Now we find the transitions T_1 and T_2 in the new timescale to calculate the new distance $\Delta\tau = 0.6876$ and repeat the calculation in 4.2.1. We use equation (4.12) to transform into the frequency space where we find the new FSR for each peak. As can be seen in figure 4.12 the so obtained array of values now has no longer a linear trend and in average results in $\mathrm{FSR}_{\mathrm{cavity}} = 940(2)\,\mathrm{MHz}$. This is within uncertainty boundaries of the theoretically calculated $\mathrm{FSR}_{\mathrm{cavity}} = 937(3)\,\mathrm{MHz}$. The slightly higher uncertainty compared to the ULE approach can be accounted to the lower thermal stability of this cavity.

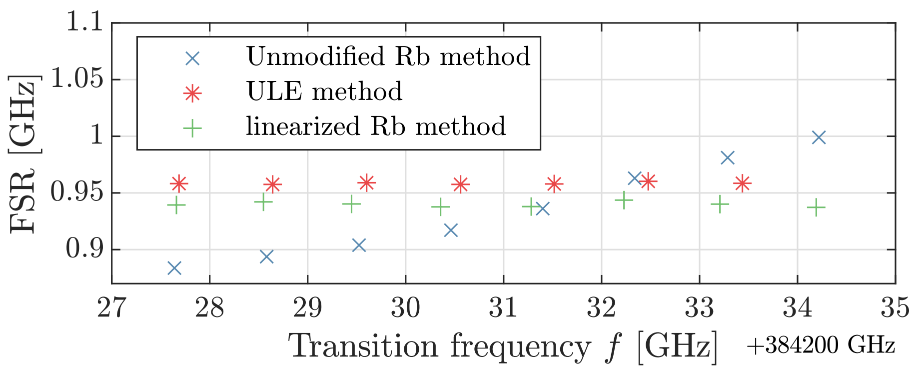

Figure 4.12.: The FSR calculated at different transition frequencies of ^{87}Rb with the three different methods presented in the text.

4.2.4. Summary

To characterize the cavity built in this thesis, we used three different methods to measure the FSR:

Unmodified Rb: Measuring the cavity modes at the same time as the rubidium D2 line transition.

ULE: Measuring the cavity modes at the same time as another cavity with a roughly known FSR = 1.5 GHz and using a polynomial to consider scanning non-linearity.

Linearized Rb: Converting the non-linear timescale to one in which cavity modes are distributed linearly and locate known Rb transitions in the new timescale.

These three approaches result in FSRs as shown in figure 4.12 and the mean values listed in table 4.1. The unmodified approach yields a higher standard deviation but is similar to the linearized Rb method and the theoretical value. The ULE method and the linearized Rb method both have low standard deviation but the ULE method yields a different result. This difference can be explained when considering that the FSR calculated with the ULE method is directly dependent on the FSR of the ULE cavity itself. For $\mathrm{FSR_{ULE}} = 1.471(6)$ GHz both results would be equal. Given that only the manufacturer specification of 1.5 GHz but no certainty is known, while the rubidium values are extremely well known, this seems to be the true FSR of the ULE cavity. Of course the linearized Rb approach could also be used to measure the FSR of the ULE.

Table 4.1.: Comparison of the mean FSR and its standard deviation for different methods of calculation.

Method	FSR [MHz]	ΔFSR [MHz]
Unmodified Rb	935	43
ULE	958	1
linearized Rb	940	2

5. Summary and Outlook

In the scope of this thesis a laser system at 835 nm for the excitation of $\mathrm{H}\,^2\Sigma^+, \mathrm{H}'\,^2\Pi$ states to Rydberg states has been planned and set up partially. A tapered amplifier (TA) has been assembled from parts and the control unit has been calibrated and set up. A protection circuit has been build and tested for functionality. The expected over voltage protection and low pass filtering was observed successfully. Consecutively, the optical parts have been set up. After the beam of the diode laser has been shaped to fit the amplifier chip,

A reference cavity for wavelength stabilization has been assembled after the design of Christian Tomschitz [1] and characterized for its free spectral range (FSR) using the molecular transitions of ^{87}Rb. The FSR that has been calculated with this method FSR = 935(43) MHz yields a high uncertainty because of nonlinear laser scanning. Another approach was used which compares transmittance of the cavity with that of a characterized ultra low expansion cavity which yields an FSR of 958(1) MHz. However, this value implies that the cavity would be 3.5 mm smaller than it should. Another linearization procedure has been developed to account for non-linearities occurring during the scanning of the ^{87}Rb. A second approach has been developed which linearizes the absorption spectrum of ^{87}Rb. This yields FSR = 940(2) MHz. Comparison of the two approaches implies that a more precise value for the FSR of the ultra low expansion cavity is FSR = 1.471(6) GHz.

From the seed Laser two beams have been refracted to the reference cavity and to a multimode fiber. Once this was done successfully, coupling into the tapered amplifier was attempted unsuccessfully. After a long troubleshooting period, it has been found that the original TA-chip was damaged, and a new chip was ordered. We anticipate that the damage was of thermal nature and might have originated from improper soldering. Unfortunately, after setting up a new chip, coupling was still unsuccessful. Numerous combinations of seed shapes and input lenses have been tested to no avail. During the frequent setup, a strategic approach for quick lens positioning and beam alignment has been developed, but many other approaches have been tried by different coworkers as well. All with the same observation: After initial beam alignment, an increase in output power is visible. As it depends on the polarity, we can confirm that it is not a back reflection, but stimulated laser emission. However, after careful and thorough optimization of lens position and beam alignment the maximum output does not exceed 80% of the seed power, even for high currents > 1.5 A. The cause could not be identified within the time available for this thesis. One hypothesis is that the developed approach does not calibrate the lens position well enough. Possibly the correct position can be identified as the point, where the amplified spontaneous emission does not change its position when the lens is turned in or out. This was investigated briefly but as this idea was developed towards the very end of this thesis, such a position has not yet been found. As an example for the characterization process we present the characterization of the TA from a functional setup instead.

In the near future, other coworkers will continue to improve the lens position and hopefully will be able to achieve amplification. Once the TA is finally set up, all wavelengths necessary for the three level excitation scheme of nitric oxide for trace gas sensing are available. In the next step, a gas mixing device has to be realized which will create a nitrogen and nitric oxide mixture with known concentrations. Then, a prototype of the ionization chamber has to be realized where the gas mixture can be investigated in through-flow.

A. Construction plans for the TA body

The here presented TA design has been used multiple times in our institute, and is easy do construct. For future references, we include all necessary schematics in this appendix. It might be possible that minor changes on the main piece or the lens tubes are needed for different chips.

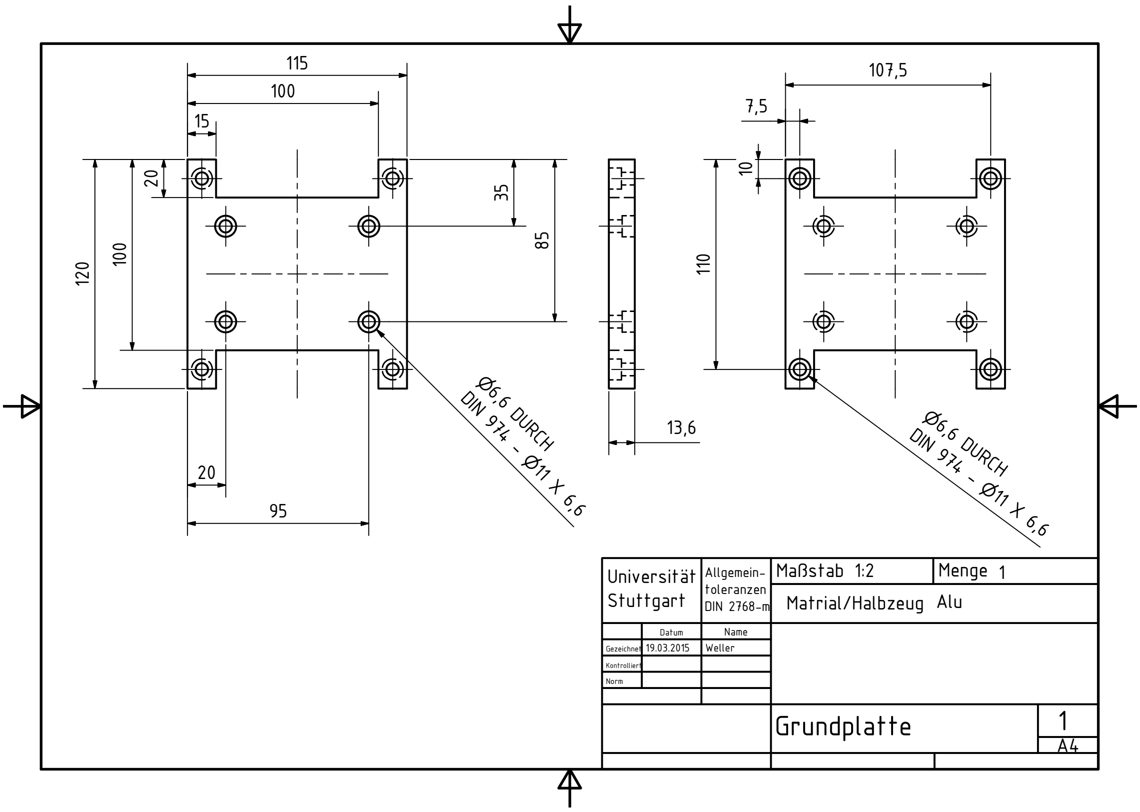

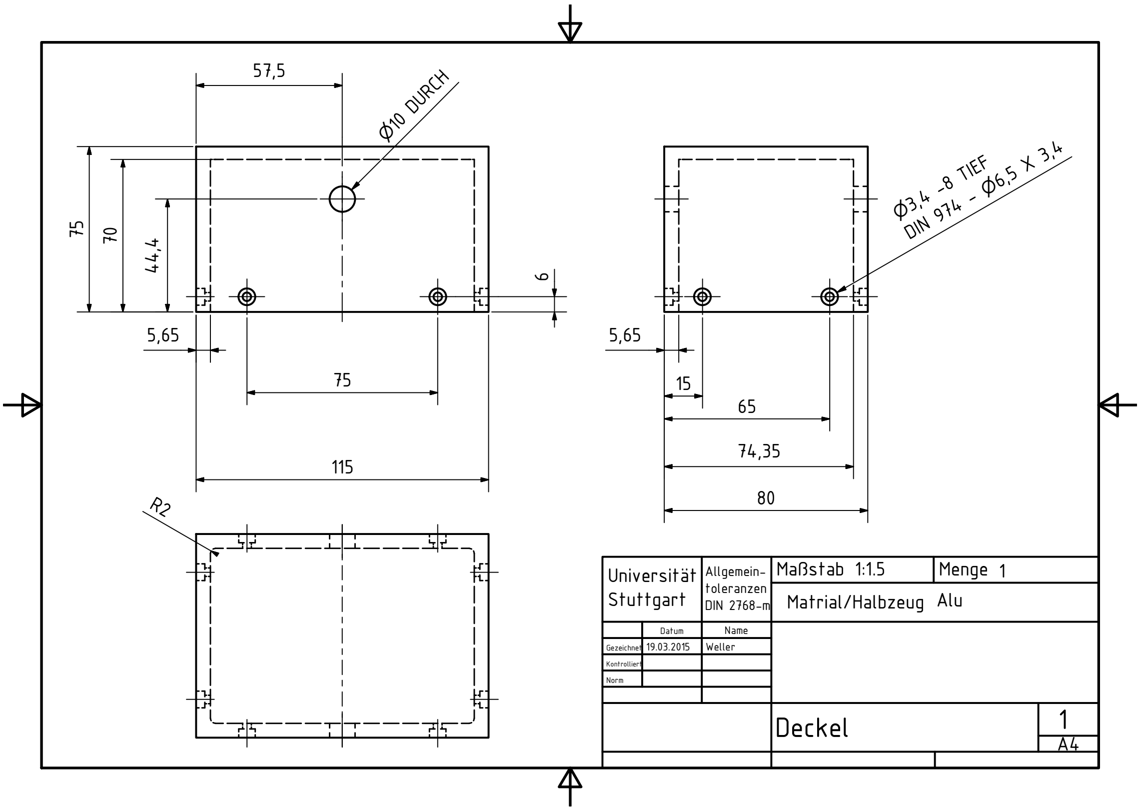
57,5
Ø10 DURCH
Ø3,4 -8 TIEF
DIN 974 - Ø6,5 X 3,4
75
70
44,4
6
5,65
75
115
15
65
74,35
80
R2
Universität Stuttgart
Allgemein-toleranzen DIN 2768-m
Maßstab 1:1.5
Menge 1
Matrial/Halbzeug Alu
Datum
Name
Gezeichnet 19.03.2015 Weller
Kontrolliert
Norm
Deckel
1
A4

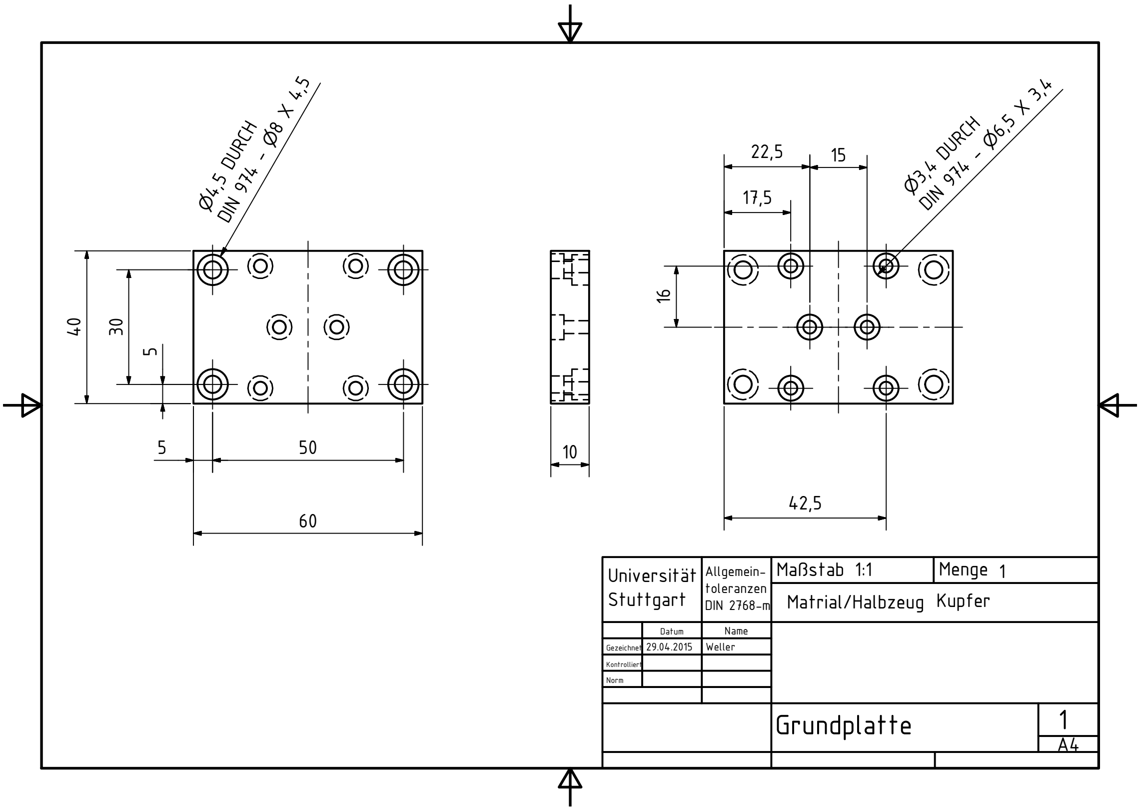
Ø4,5 DURCH
DIN 974 - Ø8 X 4,5
Ø3,4 DURCH
DIN 974 - Ø6,5 X 3,4
22,5
15
17,5
16
40
30
5
5
50
60
10
42,5
Universität Stuttgart
Allgemein-toleranzen DIN 2768-m
Maßstab 1:1
Menge 1
Matrial/Halbzeug Kupfer
Datum
Name
Gezeichnet 29.04.2015 Weller
Kontrolliert
Norm
Grundplatte
1
A4

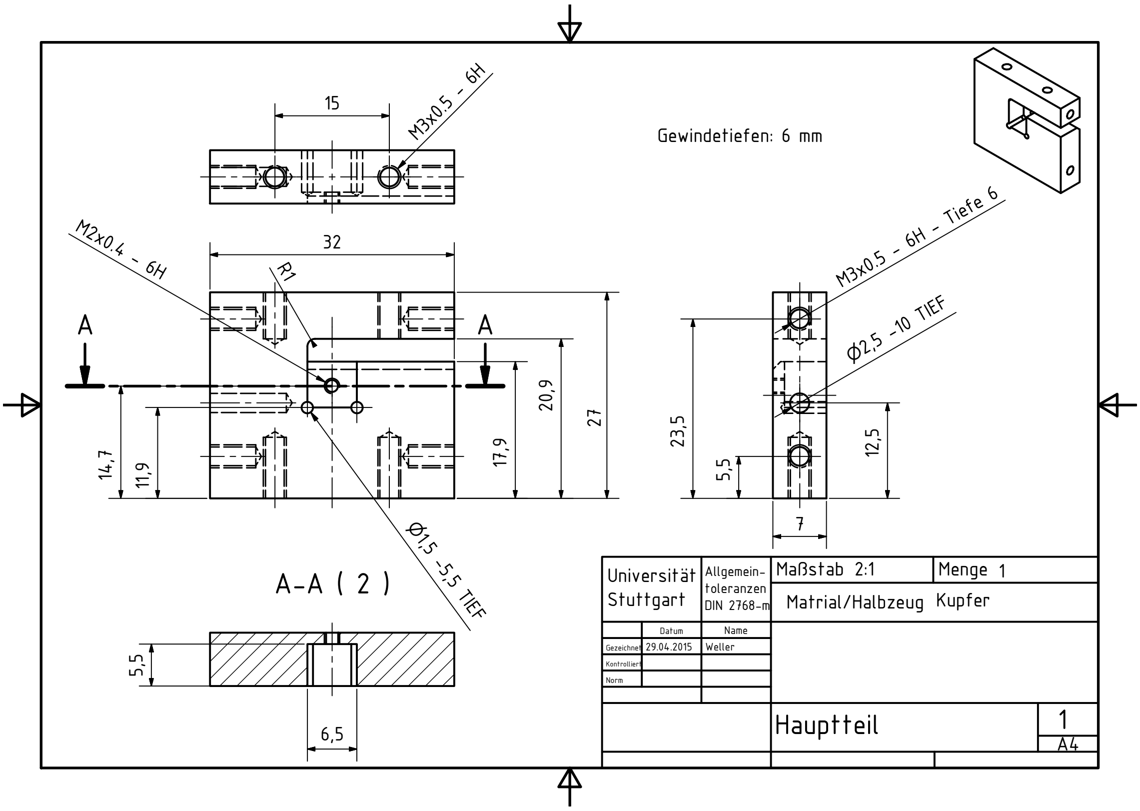
Gewindetiefen: 6 mm
M3x0.5 - 6H
M2x0.4 - 6H
M3x0.5 - 6H - Tiefe 6
Ø2,5 -10 TIEF
Ø1,5 -5,5 TIEF
A-A (2)
Universität Stuttgart
Allgemeintoleranzen DIN 2768-m
Maßstab 2:1
Menge 1
Matrial/Halbzeug Kupfer
Datum
Name
Gezeichnet 29.04.2015 Weller
Kontrolliert
Norm
Hauptteil
1
A4

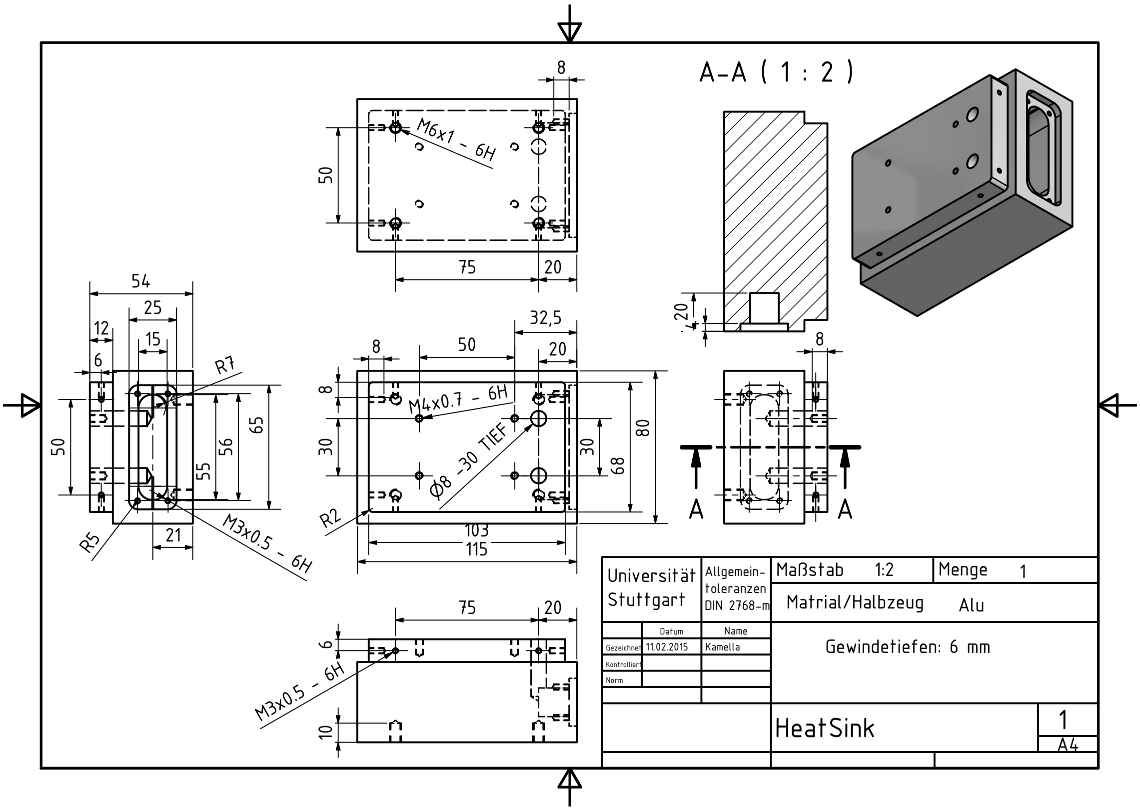
A-A (1 : 2)
M6x1 - 6H
M4x0.7 - 6H
Ø8 -30 TIEF
M3x0.5 - 6H
Universität Stuttgart
Allgemeintoleranzen DIN 2768-m
Maßstab 1:2
Menge 1
Matrial/Halbzeug Alu
Datum
Name
Gezeichnet 11.02.2015 Kamella
Kontrolliert
Norm
Gewindetiefen: 6 mm
HeatSink
1
A4

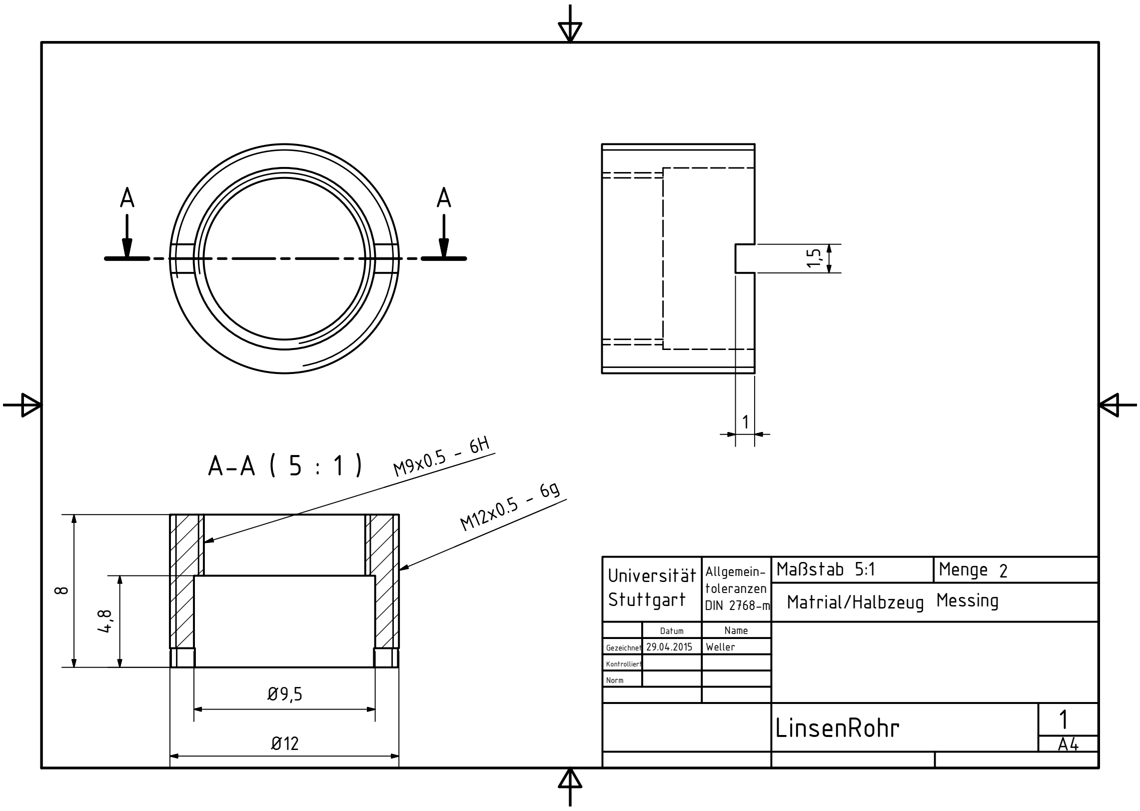
A
A
1,5
1
A-A (5 : 1)
M9x0.5 - 6H
M12x0.5 - 6g
8
4,8
Ø9,5
Ø12
Universität Stuttgart
Allgemein-toleranzen DIN 2768-m
Maßstab 5:1
Menge 2
Matrial/Halbzeug Messing
Datum
Name
Gezeichnet 29.04.2015 Weller
Kontrolliert
Norm
LinsenRohr
1
A4

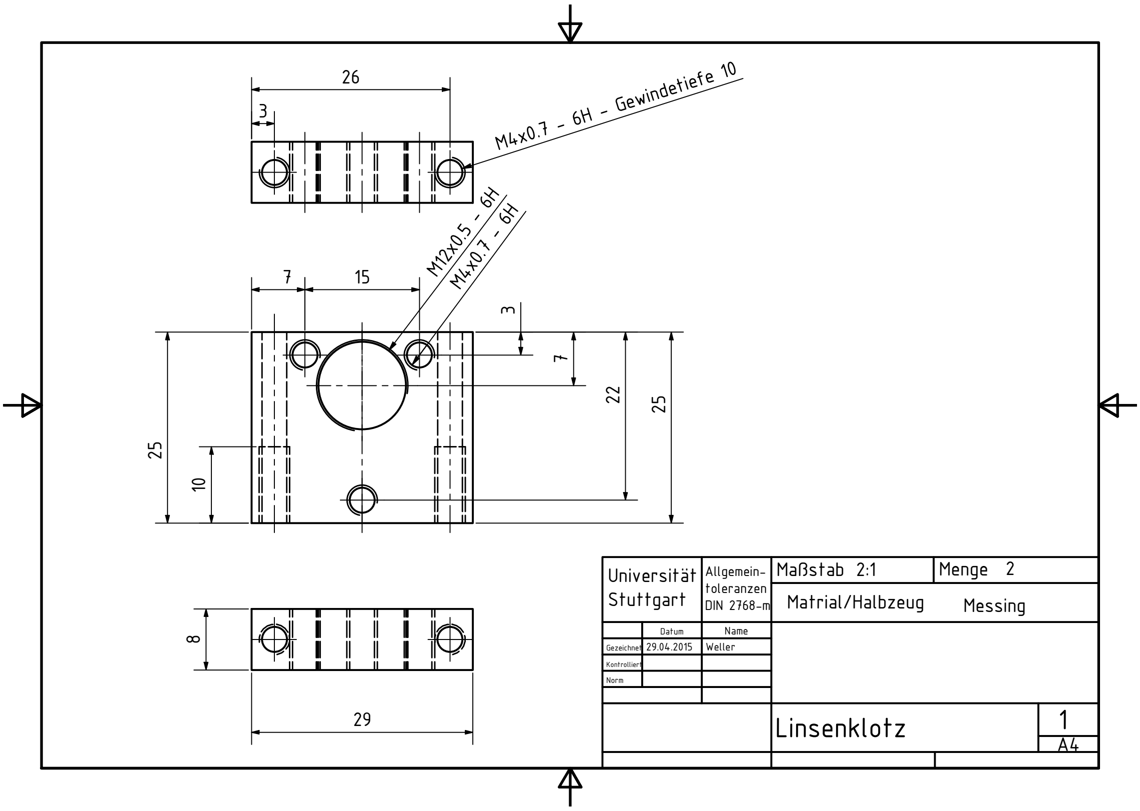
26
3
M4x0.7 - 6H - Gewindetiefe 10
M12x0.5 - 6H
M4x0.7 - 6H
7
15
3
7
22
25
25
10
8
29
Universität Stuttgart
Allgemein-toleranzen DIN 2768-m
Maßstab 2:1
Menge 2
Matrial/Halbzeug Messing
Datum
Name
Gezeichnet 29.04.2015 Weller
Kontrolliert
Norm
Linsenklotz
1
A4

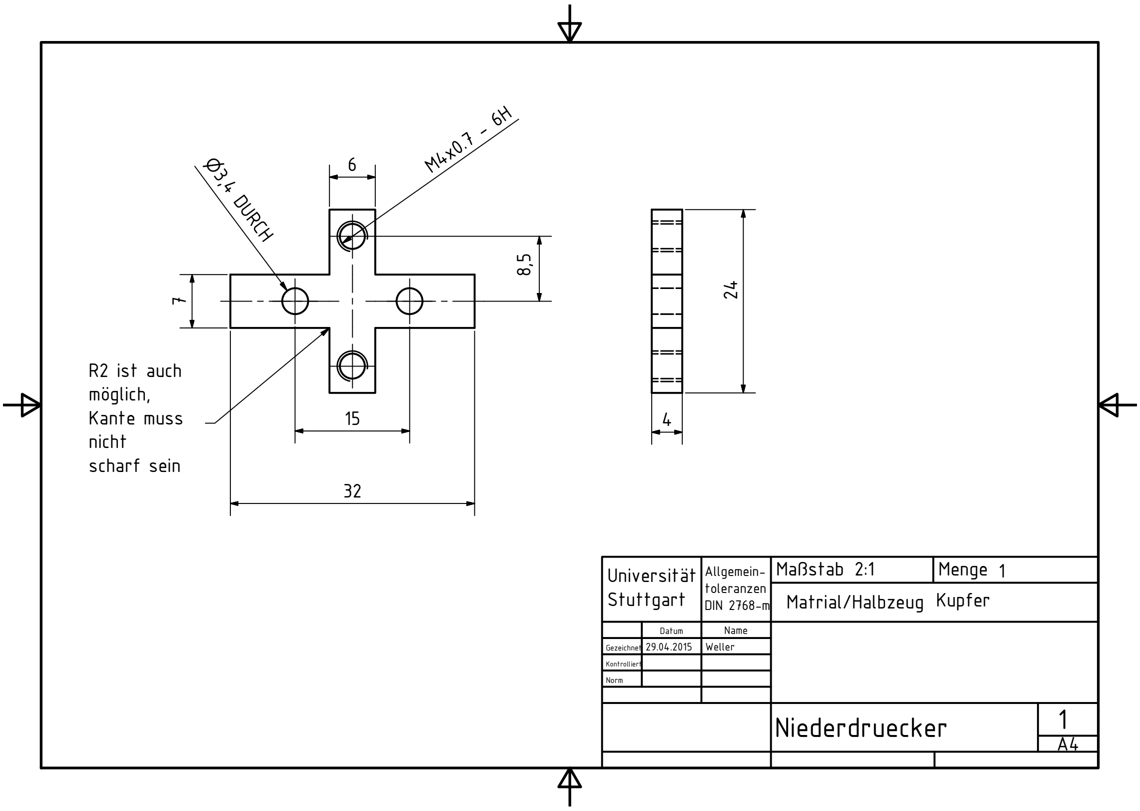
Ø3,4 DURCH
6
M4x0.7 - 6H
8,5
7
24
R2 ist auch möglich, Kante muss nicht scharf sein
15
4
32
Universität Stuttgart
Allgemein-toleranzen DIN 2768-m
Maßstab 2:1
Menge 1
Matrial/Halbzeug Kupfer
Datum
Name
Gezeichnet 29.04.2015 Weller
Kontrolliert
Norm
Niederdruecker
1
A4

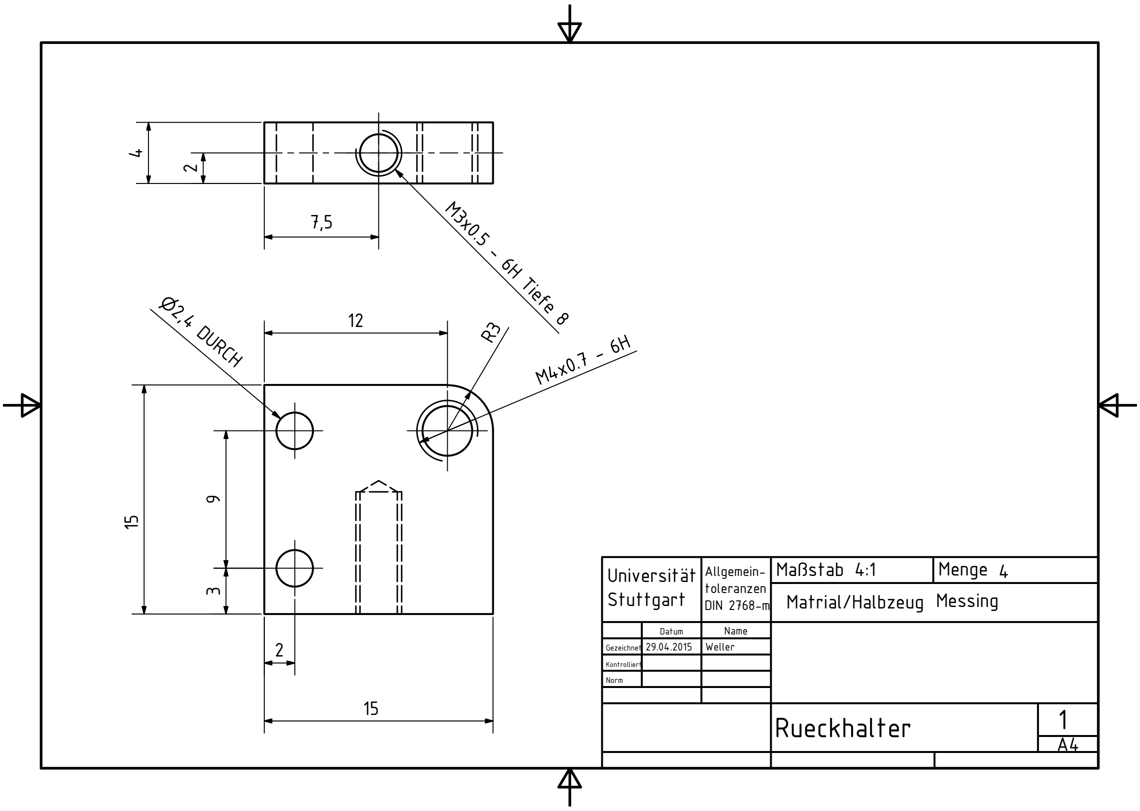
4
2
7,5
M3x0,5 - 6H Tiefe 8
Ø2,4 DURCH
12
R3
M4x0.7 - 6H
15
9
3
2
15
Universität Stuttgart
Allgemein-toleranzen DIN 2768-m
Maßstab 4:1
Menge 4
Matrial/Halbzeug Messing
Datum
Name
Gezeichnet 29.04.2015 Weller
Kontrolliert
Norm
Rueckhalter
1
A4

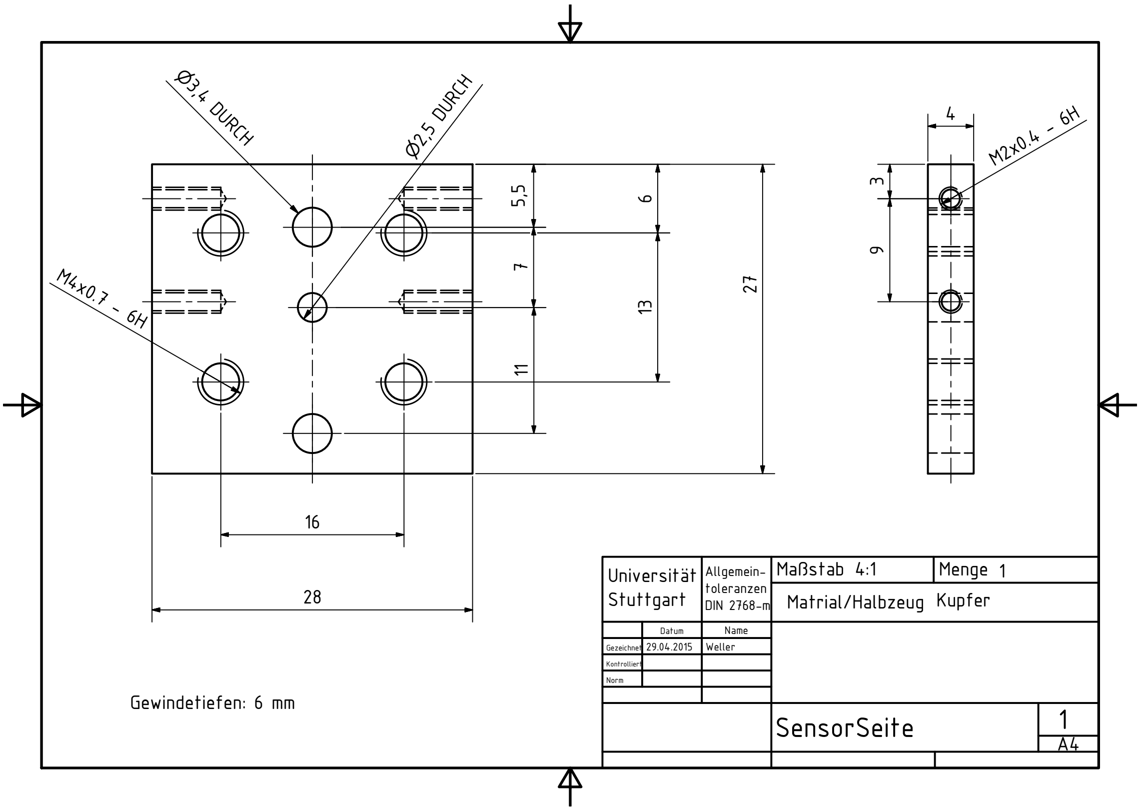
Ø3,4 DURCH
Ø2,5 DURCH
M4x0.7 - 6H
M2x0.4 - 6H
5,5
7
11
6
13
27
4
3
9
16
28
Universität Stuttgart
Allgemeintoleranzen DIN 2768-m
Maßstab 4:1
Menge 1
Matrial/Halbzeug Kupfer
Datum
Name
Gezeichnet 29.04.2015 Weller
Kontrolliert
Norm
Gewindetiefen: 6 mm
SensorSeite
1
A4

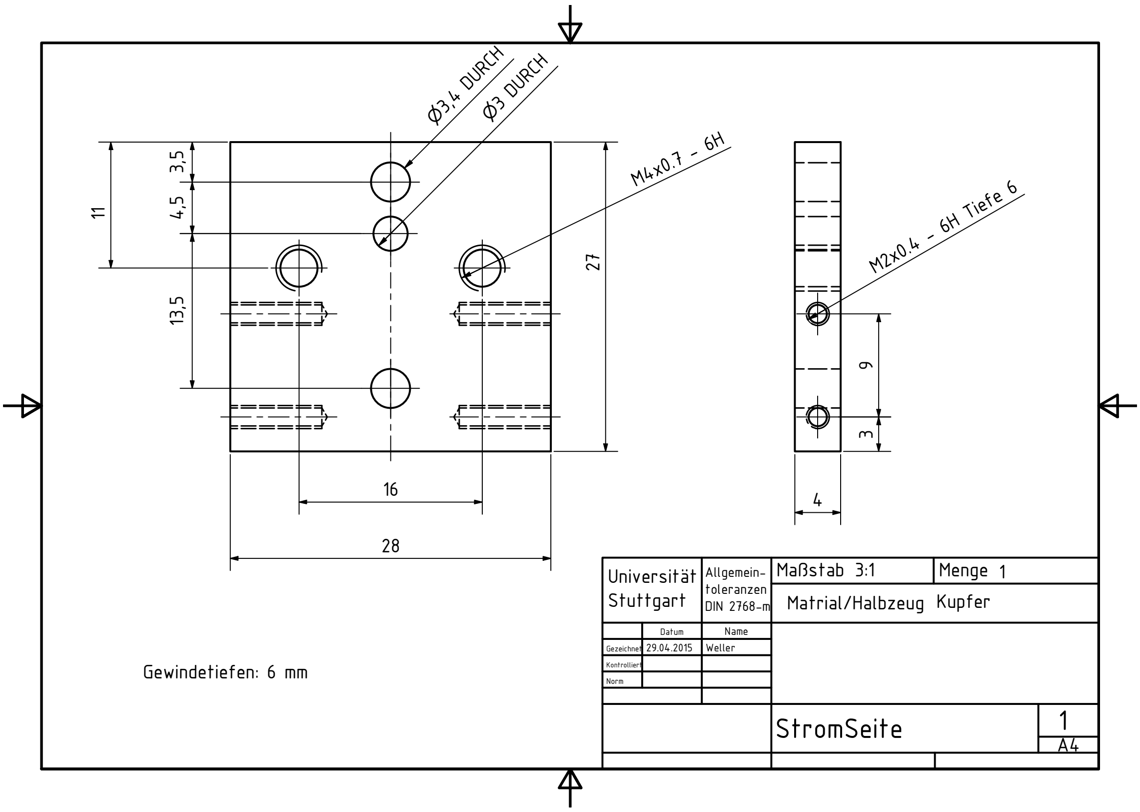
Ø3,4 DURCH
Ø3 DURCH
M4x0.7 - 6H
M2x0.4 - 6H Tiefe 6
11
3,5
4,5
13,5
27
9
3
4
16
28
Universität Stuttgart
Allgemeintoleranzen DIN 2768-m
Maßstab 3:1
Menge 1
Matrial/Halbzeug Kupfer
Datum
Name
Gezeichnet 29.04.2015 Weller
Kontrolliert
Norm
Gewindetiefen: 6 mm
StromSeite
1
A4

B. Tapered amplifier data sheet

Version 0.90 18.09.2008 page: 1 from 4

TAPERED AMPLIFIER

GaAs Semiconductor Laser Diode

RWE/RWL BAL DFB/DBR TPL/TPA

PRELIMINARY SPECIFICATION Tapered Amplifier

EYP-TPA-0830-01000-4006-CMT04-0000

General Product Information

Product	Application
830 nm Tapered Amplifier	Spectroscopy
C-Mount Package	Metrology

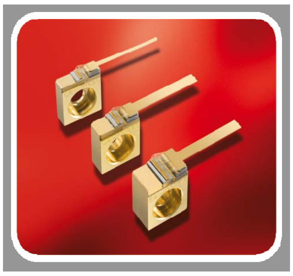

Absolute Maximum Ratings

	Symbol	Unit	min	typ	max	
Storage Temperature	T_S	°C	-40		85	non condensing
Operational Temperature at Case	T_C	°C	0		50	non condensing
Current	I_F	A			3	Stress in excess of the Absolute Maximum Ratings can cause permanent damage to the device. Operation at the Absolute Maximum Rating for extended periods of time can adversely affect the device realibility and may lead to reduced operational life.
Reverse Voltage	V_R	V			0	
Output Power	Popt	W			1.1	

Recommended Operational Conditions

	Symbol	Unit	min	typ	max	
Operational Temperature at Case	T_C	°C	5		40	non condensing
Forward Current	$I_{F\ Gain}$	A			2.5	
Input Power	P_{input}	mW	10		50	
Output Power	P_{opt}	W			1.0	with proper injection from a seed laser

Characteristics at T_{amb} 25 °C at Begin Of Life

Parameter	Symbol	Unit	min	typ	max	Measurement Conditions / Comments
Center Wavelength	λ_C	nm		830		
Gain Width (FWHM)	$\Delta\lambda$	nm		30		
Temperature Coefficient of Wavelength	$d\lambda$ / dT	nm / K		0.3		
Amplification		dB		13		
Operational Current @ P_{opt} = 1 W	$I_{op\ Gain}$	A			2.5	with proper injection from a seed laser

eagleyard Photonics GmbH
Rudower Chaussee 29 (IGZ)
12490 Berlin GERMANY
fon +49. 30. 6392 4520
fax +49. 30. 6392 4529
info@eagleyard.com
www.eagleyard.com

eagleyard PHOTONICS We focus on power.

Version 0.90 18.09.2008 page: 2 from 4

TAPERED AMPLIFIER
GaAs Semiconductor Laser Diode

RWE / RWL BAL DFB / DBR TPL / TPA

PRELIMINARY SPECIFICATION **Tapered Amplifier**

EYP-TPA-0830-01000-4006-CMT04-0000

Characteristics at T_{amb} 25 °C at Begin Of Life

Parameter	Symbol	Unit	min	typ	max	Measurement Conditions / Comments
Output Power @ I_F = 2.5 A	P_{opt}	W	1			with proper injection from a seed laser
Cavity Length	L	µm		4000		
Input Aperture (at rear side)	d_{input}	µm		3		
Output Aperture (at front side)	d_{output}	µm		200		
Astigmatism	A	µm			600	depending on operating conditions
Divergence parallel (FWHM)	$\Theta_{\|\|}$	°		14		
Divergence perpendicular (FWHM)	$\Theta_{\perp}$	°		28		
Polarization				TE		E field parallel to junction plane

eagleyard Photonics GmbH Rudower Chaussee 29 (IGZ) 12490 Berlin GERMANY fon +49. 30. 6392 4520 fax +49. 30. 6392 4529 info@eagleyard.com www.eagleyard.com

eagleyard PHOTONICS We focus on power.

TAPERED AMPLIFIER
GaAs Semiconductor Laser Diode

RWE / RWL BAL DFB / DBR TPL / TPA

PRELIMINARY SPECIFICATION Tapered Amplifier

EYP-TPA-0830-01000-4006-CMT04-0000

Package Dimensions

	Symbol	Unit	min	typ	max
Emission Plane	l	mm	7.05	7.20	7.35
C-Mount Thickness	d	mm		4.15	

Package Pinout

Cathode (-)	Mounting Wire
Anode (+)	Housing

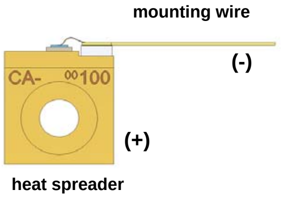

Package Drawings

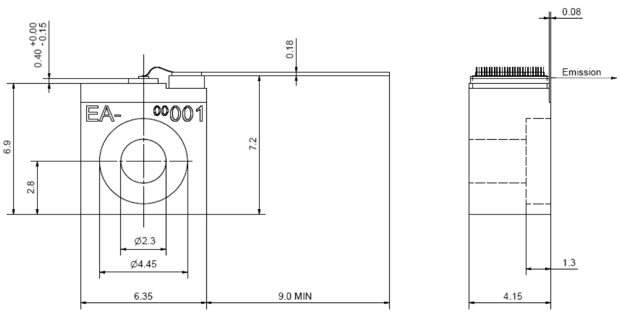

eagleyard Photonics GmbH
Rudower Chaussee 29 (IGZ)
12490 Berlin GERMANY
fon +49. 30. 6392 4520
fax +49. 30. 6392 4529
info@eagleyard.com
www.eagleyard.com

We focus on power.

TAPERED AMPLIFIER

GaAs Semiconductor Laser Diode

PRELIMINARY SPECIFICATION **Tapered Amplifier**

EYP-TPA-0830-01000-4006-CMT04-0000

Typical Measurement Results

Spectrum measured w/o injection:

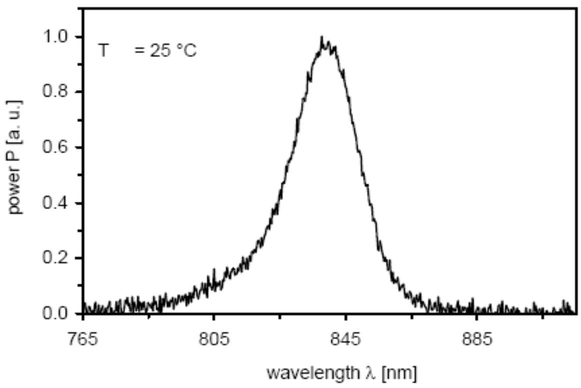

Performance figures, data and any illustrative material provided in this specification are typical and must be specifically confirmed in writing by eagleyard Photonics before they become applicable to any particular order or contract. In accordance with the eagleyard Photonics policy of continuous improvement specifications may change without notice.

Unpacking, Installation and Laser Safety

Unpacking the laser diodes should only be done at electrostatic safe workstations (EPA). Though protection against electro static discharge (ESD) is implemented in the laser package, charges may occur at surfaces. Please store this product in its original package at a dry, clean place until final use. During device installation, ESD protection has to be maintained.

The TPA diode type is known to be sensitive against thermal stress. It should not be operated without appropriate injection from a seed laser. Operating at moderate temperatures on propper heat sinks willl contribute to a long lifetime of the diode.

The laser emission from this diode is close to the invisible infrared region of the electromagnetic spectrum. Avoid direct and/or indirect exposure to the free running beam. Collimating the free running beam with optics as common in optical instruments will increase thread to the human eye.

Each laser diode will come with an individual test protocol verifying the parameters given in this document.

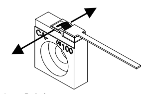

Laser Emission

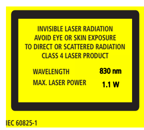

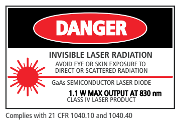

eagleyard Photonics GmbH
Rudower Chaussee 29 (IGZ)
12490 Berlin GERMANY
fon +49. 30. 6392 4520
fax +49. 30. 6392 4529
info@eagleyard.com
www.eagleyard.com

We focus on power.

C. Functions for timescale linearization

Here we provide two Matlab™ functions that can be used to use the nonlinear time scale which often is produced when using a laser to scan through a range of wavelengths. They both need to be given points on the time scale (such as from a cavity) that should be linearly distributed. The first function can be used when the peak distance in the frequency scale is known, to directly convert the timescale into a frequency scale.

Algorithmus C.1

```
function f = linearizeFrequency(time, peakIndex, frequencyDistance)
% this function creates a linear frequency scale from a nonlinear
% timescale % with peak locations when the distance of those peaks
% in the frequency scale is known.

ULEFSR = frequencyDistance*(1:length(peakIndex))';
myFit = fit(time(peakIndex), ULEFSR, 'poly4');
f = polyval(coeffvalues(myFit), time);

end
```

where the positions of the peaks in the new frequency scale `f` are now distributed equidistantly. The second function transforms the time scale into a linear time scale, where the return value `t` is a new linearized timescale, in which the index of one point in the old timescale corresponds to the same index in the new timescale.

Algorithmus C.2

```
function t = linearizeTime(time, peakIndex)
% this function linearizes and normalizes a timescale, so that peaks
% that were unevenly distributed are now distributed evenly.

distance = mean(time(peakIndex(3:end))-time(peakIndex(1:end-2))/2);
startTime = time(peakIndex(1));

equidistantPeaks = (startTime:distance:9*distance+startTime)';
myFit = fit(peakIndex, equidistantPeaks, 'poly4');

t = polyval(coeffvalues(myFit), time);
t = linearizedTime-min(linearizedTime);
t = linearizedTime/max(linearizedTime);
end
```

Bibliography

[1] Christian Tomschitz. *A photoionization scheme to create cold ionic impurities fom Rydberg atoms.* Masters thesis, University of Stuttgart, Stuttgart, 2018.

[2] H. Y. Yun, V. L. Dawson, and T. M. Dawson. Neurobiology of nitric oxide. *Critical reviews in neurobiology*, 10(3-4):291–316, 1996. ISSN 0892-0915. doi: 10.1615/critrevneurobiol.v10.i3-4.20.

[3] S. Moncada and E. A. Higgs. The discovery of nitric oxide and its role in vascular biology. *British journal of pharmacology*, 147 Suppl 1:S193–201, 2006. ISSN 0007-1188. doi: 10.1038/sj.bjp.0706458.

[4] Douglas D. Thomas, Lisa A. Ridnour, Jeffrey S. Isenberg, Wilmarie Flores-Santana, Christopher H. Switzer, Sonia Donzelli, Perwez Hussain, Cecilia Vecoli, Nazareno Paolocci, Stefan Ambs, Carol A. Colton, Curtis C. Harris, David D. Roberts, and David A. Wink. The chemical biology of nitric oxide: implications in cellular signaling. *Free radical biology & medicine*, 45(1):18–31, 2008. ISSN 0891-5849. doi: 10.1016/j.freeradbiomed.2008.03.020.

[5] M. Jorissen, L. Lefevere, and T. Willems. Nasal nitric oxide. *Allergy*, 56(11): 1026–1033, 2001. ISSN 0105-4538. doi: 10.1034/j.1398-9995.2001.00145.x.

[6] Sheetal Korde Choudhari, Minal Chaudhary, Sachin Bagde, Amol R. Gadbail, and Vaishali Joshi. Nitric oxide and cancer: a review. *World journal of surgical oncology*, 11:118, 2013. doi: 10.1186/1477-7819-11-118.

[7] J. O. Lundberg, E. Weitzberg, J. M. Lundberg, and K. Alving. Nitric oxide in exhaled air. *The European respiratory journal*, 9(12):2671–2680, 1996. ISSN 0903-1936. doi: 10.1183/09031936.96.09122671.

[8] Johannes Schmidt. *A trace gas sensor based on Rydberg excitations.* Phd, University of Stuttgart, Stuttgart, 2019.

[9] J. Schmidt, M. Fiedler, R. Albrecht, D. Djekic, P. Schalberger, H. Baur, R. Löw, N. Fruehauf, T. Pfau, J. Anders, E. R. Grant, and H. Kübler. Proof of concept for an optogalvanic gas sensor for no based on rydberg excitations. *Applied Physics Letters*, 113(1):011113, 2018. ISSN 0003-6951. doi: 10.1063/1.5024321. URL `https://aip.scitation.org/doi/pdf/10.1063/1.5024321`.

[10] Fabian Munkes. *Continuous-wave absorption spectroscopy on the* $X\,^2\Pi_{1/2}$ *to* $A\,^2\Sigma^+$ *transition of nitric oxide.* `Master's dissertation,` University of Stuttgart, October 2019. URL `https://www.pi5.uni-stuttgart.de/documents/abgeschlossene-arbeiten/`

2019-Munkes-Fabian-Continuous-wave-absorption-spectroscopy-on-the-X2Pi1_ 2-to-A2Sigma-transition-of-nitric-oxide-MSc.pdf.

[11] André Bisquerra. *Setup and Characterisation of a Frequency-Doubled Laser-system for Spectrscoopy of the* $A^2\Sigma^+$ *to* $H^2\Sigma^+$ *Transition in Nitric Oxide*. Bachelor thesis, University of Stuttgart, Stuttgart, October 2019. URL https://www.pi5.uni-stuttgart.de/documents/abgeschlossene-arbeiten/2019-Bisquerra-Andre-Setup-and-Characterisation-of-a-Frequency-Doubled-Lasersystem- ..-BSC.pdf.

[12] Jayampathi C. B. Kangara, Andrew J. Hachtel, Matthew C. Gillette, Jason T. Barkeloo, Ethan R. Clements, Samir Bali, Brett E. Unks, Nicholas A. Proite, Deniz D. Yavuz, Paul J. Martin, Jeremy J. Thorn, and Daniel A. Steck. Design and construction of cost-effective tapered amplifier systems for laser cooling and trapping experiments. *American Journal of Physics*, 82(8):805–817, 2014. ISSN 0002-9505. doi: 10.1119/1.4867376.

[13] Ryan Cole. *Construction and optimization of a tapered amplifier system for applications in ultra-cold plasma research*. Senior honors thesis, Colby. URL https://digitalcommons.colby.edu/cgi/viewcontent.cgi?article=1759&context=honorstheses.

[14] Matthias Fucs. *Development of a high power stabilized diode laser system*. PhD thesis, University of Oregon, Oregon, June 2006. URL https://atomoptics-nas.uoregon.edu/publications/matthias-fuchs-thesis.pdf.

[15] E. Gehrig and O. Hess. Optimization of tapered semiconductor optical amplifiers for picosecond pulse amplification. *Applied Physics Letters*, 87(25):251106, 2005. ISSN 0003-6951. doi: 10.1063/1.2149177.

[16] THORLABS. Itc1xx oem laser diode controller manual, 2018. URL https://www.thorlabs.com/newgrouppage9.cfm?objectgroup_id=984.

[17] Iván D. Díaz-Rodríguez, Sangjin Han, and Shankar P. Bhattacharyya. *Analytical Design of PID Controllers*. Springer Nature Switzerland, Cham, Switzerland, 2019. ISBN 978-3-030-18228-1.

[18] Calctool: f/#, na, and spot size calculator, 5.3.2020. URL http://www.calctool.org/CALC/phys/optics/f_NA.

[19] Laser power through aperture calculator (gaussian beam) | ophir photonics, 5.3.2020. URL https://www.ophiropt.com/laser--measurement/laser-power-energy-meters/services/power-through-aperture-calculator.

[20] eagleyard. Tapered amplifier chip data sheet. URL https://www.eagleyard.com/fileadmin/downloads/data_sheets/EYP-TPA-0830-01000-4006-CMT04-0000.pdf.

[21] Jintao Fan, Wei Chen, Chenglin Gu, Youjian Song, Lu Chai, Chingyue Wang, and Minglie Hu. Noise characteristics of high power fiber-laser pumped femtosecond optical parametric generation. *Optics express*, 25(20):24594–24603, 2017. doi: 10.1364/OE.25.024594.

[22] Weng W. Chow and Stephan W. Koch. *Semiconductor-Laser Fundamentals: Physics of the Gain Materials*. Springer Berlin Heidelberg, Berlin, Heidelberg and s.l., 1999. ISBN 9783642083860. doi: 10.1007/978-3-662-03880-2.

[23] D. Voigt, E. C. Schilder, R.J.C. Spreeuw, and H. B. van Linden Heuvell. Characterization of a high-power tapered semiconductor amplifier system. *Applied Physics B*, 72(3):279–284, 2001. ISSN 0946-2171. doi: 10.1007/s003400100513.

[24] Ayan Banerjee and Vasant Natarajan. Saturated-absorption spectroscopy: Eliminating crossover resonances by use of copropagating beams. *Optics Letters*, 28(20):1912–1914, 2003. ISSN 0146-9592. doi: 10.1364/OL.28.001912.

[25] S. Bize, Y. Sortais, M. S. Santos, C. Mandache, A. Clairon, and C. Salomon. High-accuracy measurement of the 87 rb ground-state hyperfine splitting in an atomic fountain. *Europhysics Letters (EPL)*, 45(5):558–564, 1999. ISSN 0295-5075. doi: 10.1209/epl/i1999-00203-9.

[26] J. Ye, S. Swartz, P. Jungner, and J. L. Hall. Hyperfine structure and absolute frequency of the (87)rb 5p(3/2) state. *Optics Letters*, 21(16):1280–1282, 1996. ISSN 0146-9592. doi: 10.1364/ol.21.001280.

[27] Daniel A. Steck. Rubidium 87 D line data. 21 November 2019. URL `https://www.pi5.uni-stuttgart.de/documents/abgeschlossene-arbeiten/2019-Schmidt-Johannes-A-trace-gas-sensor-based-on-Rydberg-excitations-PhD.pdf`.

Nomenclature

ASE	Amplified spontaneous emission
CA	Clear aperture
EFL	Effective focal length
NA	Numerical aperture
PBS	Polarizing beamsplitter
ULE	Ultra low expansion